Technical University of Denmark

DTU

Transformations and Evolution of Phase Singularities in Diffracted Optical Vortices

Bekshaev, A. Ya.; Angelsky, Oleg V.; Hanson, Steen Grüner

Published in:
Advances in Optics: Reviews

Publication date:
2018

Document Version
Publisher's PDF, also known as Version of record

[Link back to DTU Orbit](#)

DTU Library
Technical Information Center of Denmark

Chapter 13
Transformations and Evolution of Phase Singularities in Diffracted Optical Vortices

A. Bekshaev, O. Angelsky and S. G. Hanson

13.1. Introduction

Diffraction is one of the most traditional and deeply investigated phenomena of classical optics [1, 2], and it is difficult to believe that its further study can bring any peculiar news on the physical features of optical fields. Of course, there are many quantitative details and special cases of diffraction that still need refinement and further elucidation but the general principles of diffracted field formation and evolution seem to be firmly established and widely known. However, this is not the case with structured light fields that have become a hot topic of modern optics during the past decades [3], especially with light beams carrying optical vortices (OV) [4–6]. The edge diffraction of circular OV beams [7–23] shows many impressive non-trivial details associated with their special physical attributes: helical wavefront shape and transverse energy circulation. In case of the OV beam diffraction, common and well-studied diffraction effects (fringes, transverse diffusion of the light energy, etc. [1, 2]) are supplemented with the OV-specific diffraction transformations which seem bizarre and surprising at first glance. The first of such effects is the asymmetric penetration of light energy into the shadow region [9, 13–18] impressively testifying for the transverse energy circulation in the incident beam, which comes to light due to the beam symmetry violation caused by the diffraction obstacle [16] (see Fig. 13.2 below for an example). Beside this, much attention was recently paid to the distribution and migration of the OVs within the diffracted beam [7, 8, 11, 12, 14–15, 19–21]; especially, it was shown that even if the incident OV is stopped by the obstacle, it is restored after a certain propagation distance (OV regeneration [7, 8, 10, 19]). The interest to the OVs in the diffracted beams is supported by the peculiar character of the OV cores as amplitude zeros and phase singularities, whereby they are physically highlighted and can be precisely detected and localized [24–28], which is employed, e.g., in sensitive metrology [29–32].

A. Bekshaev
Odessa I. I. Mechnikov National University, Odessa, Ukraine

It is well established, both theoretically and in experiment, that after diffraction of an incident circular OV beam, at which its singular point is not 'screened' by the obstacle, the OV core shifts from its initial axial position, and an *m*-charged OV is decomposed into a set of |*m*| secondary single-charged ones thus forming the 'singular skeleton' [6] of the diffracted beam. During propagation of the diffracted beam, the OV cores move along intricate spiral-like trajectories [19, 23] carrying distinct 'fingerprints' of the incident beam and its disposition with respect to the diffraction obstacle. A similar transformation of the singular skeleton can be observed in a fixed cross section of the diffracted beam when the screen edge performs a monotonous translation in the transverse direction towards or away from the beam axis [20–22].

However, the singular skeleton evolution is not limited by the 'smooth' migration of the secondary OVs within the diffracted beam 'body'. Generally, this process is accompanied by various topological reactions [4, 6]: the OV disappearance and regeneration [7, 8, 10], emergence of new OVs, their annihilation, etc. Normally, such events occur at the beam periphery and are related with the diffraction fringes, etc. [15, 19] but some sorts of topological reactions are intimately connected with the 'regular' OV migration and constitute its part [22]. Importantly, the progress of these reactions is highly sensitive to the incident beam properties and the diffraction conditions (e.g., the screen edge position or the propagation distance behind the screen plane). Therefore, in addition to the general physical interest, these topological events offer potentially valuable and prospective means for precise measurements and diagnostics of the OV beam's characteristics.

In this chapter, we make an effort for a systematic study of the singular skeleton formation, evolution and transformations associated with the diffraction of circular OV beams. The presentation is based mainly on the recent works [20, 21, 23, 33]. In contrast to some previous studies [7, 8, 15, 19], the consideration is mostly restricted to the case of 'weak diffraction perturbation' (WDP) when the screen edge is located far enough from the incident beam axis. We do not specify exactly which perturbation can be called 'weak'. Practically this implies that the beam visually preserves the initial circular shape immediately after the screen, which for typical OV beams takes place if the screen is separated from the axis by two or more beam radii measured at e^{-1} intensity level (see, for example, Figs. 13.17 (a) and 13.18 (a) for the illustration), but realizing that some important conclusions of the WDP-based reasoning can be applicable well beyond any formal limits of its validity. Surprisingly enough, it is the WDP situations that appear the most favourable for explicit manifestation of the OV-related phenomena in the diffracted beam singular skeleton behaviour.

We start with description of the experimental approach (Section 13.2) and of the general numerical means for the OV diffraction simulation (Section 13.3). The consideration is based on the Kummer [34] and Laguerre-Gaussian (LG) [4–6] models for the incident OV beam: the former adequately describes OV beams obtained from an initial Gaussian beam with the help of suitable vortex-generating elements widely used in experimental practice; the latter is a standard OV beam model convenient for calculations. Comparative analysis of the results obtained with the two different models will highlight the diffraction effects related to the vortex character of the incident beam 'per se' and separate them from

'occasional' consequences of the incident beam radial profile, etc. The physical nature of the diffraction-induced beam transformations is explained with the help of a simple analytical model of the diffracted field formation based on interference of the incident beam with the edge wave [2] formed due to the incident field scattered by the screen edge. The analytical model is refined by means of the asymptotic analysis of the Fresnel–Kirchhoff diffraction integral [21, 33] (Section 13.4).

Further, the developed theoretical instruments are applied to the singular skeleton analysis in the diffracted beam in both basic situations: when the screen edge is fixed but the observation plane moves along the propagation direction (z-dependent evolution, cf. Fig. 13.1) and when the observation plane is fixed and the diffracted beam structure changes due to the screen edge translation (a-dependent evolution). In Section 13.5, the simplified situation of diffraction of a low-order LG beam discloses the nature of the spiral-like OV trajectories ('vortex filaments') and its intrinsic relations with the vortex beam structure.

In the first approximation, these trajectories look smooth but further examination reveals the existence of topological discontinuities that are studied both for the LG and Kummer beams' diffraction in Sections 13.6 and 13.7. We describe the typical manifestations of such discontinuities ('jumps') as a series of topological reactions associated with the birth of the OV dipole at a remote point of the beam cross section followed by collision of one of the dipole constituents with the initial OV and their subsequent annihilation. This enabled us to introduce the numerical criterion for the OV trajectory 'jumps' whose validity is demonstrated in a number of examples of the singular skeleton transformation both for the a-dependent and z-dependent diffracted beam evolution. The observed discontinuities are also interpreted based on the transverse projections of the everywhere smooth and continuous 3D vortex filaments in the diffracted field. Possible applications of the results and the prospective lines of further research are discussed in the conclusion.

13.2. Experimental Setup

We start with outlining the typical experimental situation in which the OV diffraction is explored [7–15, 19, 20] (see Fig. 13.1 (a)). A circular OV beam whose axis coincides with the z-axis is directed onto the diffraction obstacle S – an opaque screen with sharp vertical edge, mounted with possibility of precise adjustment of the off-axis distance a in the horizontal x-direction. The diffracted beam formed behind the screen is observed with the help of a CCD camera positioned orthogonally to the incident OV beam axis at different adjustable distances z from the obstacle. The nature of the incident OV beam is less important; many previous works [7–13] deal with the standard Laguerre-Gaussian beams of various topological charges that are characterized by the Gaussian envelope parameters: the waist radius at e^{-1} intensity level b_0, the corresponding Rayleigh range [2]

$$z_{Rc} = k b_0^2 , \qquad (13.1)$$

and the longitudinal distance from the waist to the screen z_c (see Fig. 13.1 (b)). In particular, impressive experiments were performed by Arlt with the LG beams of zero

radial index $z_c = 0$ [9], which clearly show internal energy circulation in the OV beams. In Fig. 13.2 the original results of [9] are re-arranged according to the geometry of Fig. 13.1 (a); here, as well as in the whole chapter, all views of the beam cross section are presented as seen against the beam propagation (from the positive end of the optical axis z).
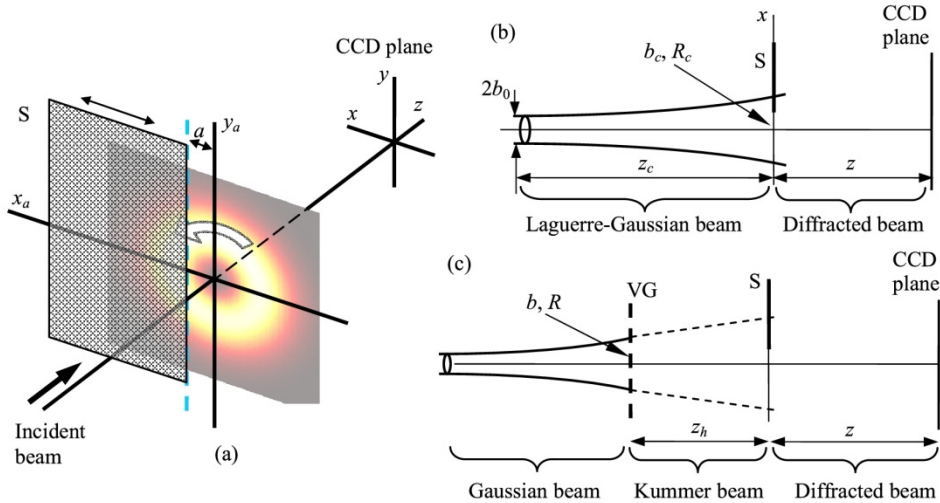

Fig. 13.1. (a) General view of the OV beam diffraction with the beam screening and the involved coordinate frames; schemes of (b) diffraction of the incident LG beam and (c) formation and diffraction of the incident Kummer beam. VG is the OV-generating element, S is the diffraction obstacle (opaque screen with the edge parallel to axis y, its position along axis x is adjustable), the diffraction pattern is registered in the observation plane by means of the CCD camera. Further explanations appear in the text.

Now our aim is to study the individual singularities of the diffracted beam rather than its general amplitude and phase profile. The adopted experimental scheme presented by Fig. 13.1 (c) [20] includes the He-Ne laser (wavelength $\lambda = 633$ nm, wavenumber $k = 2\pi/\lambda \simeq 10^5$ cm^{-1}) that generates a Gaussian beam with the waist plane at the laser output window where its amplitude is distributed according to the equation

$$u_0(r) \propto \exp\left(-\frac{r^2}{2b_0^2}\right),\tag{13.2}$$

with r being the radial distance from the beam axis, the waist beam radius equals $b_0 = 0.165$ mm (corresponding Rayleigh range is $z_{Rc} = 27$ cm). After passing a distance $z_0 = 27$ cm, the beam impinges on the center of the vortex-generating element VG (in [20], the holographic grating with groove bifurcation – i.e., the 'fork' hologram [4, 5]); in the grating plane, the Gaussian beam radius b and its wavefront curvature radius R are

$$b = 0.232 \text{ mm}; \quad R = 54 \text{ cm}\tag{13.3}$$

m =+4

(a) (b)
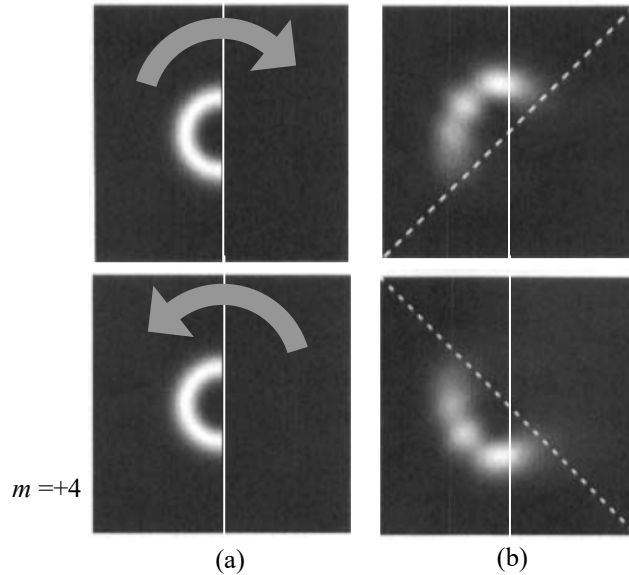
Fig. 13.2. Intensity distribution of the diffracted LG beams with the topological charge (azimuthal index) $m = \pm 4$ (the beam waist plane coincides with the screen plane S, screen edge position $a = 0$): (a) immediately behind the screen and (b) at the distance $z = z_R$ (13.1). The gray arrows show the energy circulation handedness, dotted line indicates the rotation angle 45°; the vertical line is the screen edge projection.

(the value of b defines the transverse characteristic scale for the system geometry). The holographic grating produces a 'fan' of diffracted beams, $\pm n$-th diffraction order carrying an OV beam with topological charge $\pm n$. The selected grating-generated OV beam was directed to the screen. The total distance from the grating VG to the screen S was $z_h = 11$ cm (see Fig. 13.1 (c)). In all cases, the OV beam approaching the screen plane was apparently circularly symmetric and of a negative topological charge m ($m = -1, -2, -3$); the transverse energy circulation in the screen plane is shown in Fig. 13.1 (a) by the curve arrow. The intensity profile of the diffracted beam was registered by the CCD camera with the sensitive area 4.8×3.6 mm^2, or 768×576 pixels where the pixel size is 6.25 μm.

The exact localization of the OV cores in the diffracted beam cross section is not a trivial task; usual interference methods for the OV detection (by finding the fork-like defects in the fringe pattern formed due to interference with a reference wave without wavefront dislocation [4]) are hardly applicable because of the low spatial resolution. That is why several special approaches were proposed for the OV detection. For example, we can mention the procedures employing the Shack – Hartmann wavefront testing method [24, 25], 2D analytical signal representation and interpolation ('OV metrology') [26, 27], statistical algorithms based on reconstructed OV phase maps [28], etc. Since our primary goal is to precisely locate the OV cores in conditions where their existence is doubtless, these can be detected directly from the measured intensity patterns, searching the

349

amplitude zeros [20, 21]. Their coordinates were measured automatically by averaging over 150 consecutive snapshots, which facilitated a decrease in the fluctuation instabilities. To increase the spatial resolution, an interpolation procedure was employed: the near zero intensity distribution was approximated by an asymmetric paraboloid, and the exact zero position was recognized as a center of the equal-intensity ellipses with subpixel accuracy, ~ 1 μm.

This experimental scheme is adjusted for the study of *a*-dependent evolution of the diffracted beam pattern at several fixed distances *z* behind the screen; in the special conditions of [20, 21] *z* = 30 cm, 60 cm and 82 cm.

13.3. Description of the Diffraction Model

13.3.1. General Principles of the Singular Skeleton Analysis

In conjunction with the experimental research, the diffraction of OV beams is analyzed by a mathematical model based on paraxial optics [2, 4, 5]. Let the incident monochromatic paraxial beam be described in the screen plane S (Fig. 13.1) by the slowly varying complex amplitude distribution $u_a(x_a, y_a)$; then in the observation plane at a distance *z* behind S the diffracted beam complex amplitude can be found via the Fresnel–Kirchhoff integral

$$u(x, y, z) = \frac{k}{2\pi i z} \int_{-\infty}^{\infty} dy_a \int_{-\infty}^{a} dx_a \, u_a(x_a, y_a) \exp\left\{\frac{ik}{2z}\left[(x - x_a)^2 + (y - y_a)^2\right]\right\}, \quad (13.4)$$

in any cross section, the instantaneous electric field of the paraxial beam field equals $\mathrm{Re}\left[u(x, y, z) \exp(ikz - i\omega t)\right]$ with $\omega = ck$, *c* is the velocity of light. The integral (13.4) is calculated for different input distributions $u_a(x_a, y_a)$ characterizing the typical OV beams (see below) and the resulting distribution $u(x, y, z)$ is analyzed at given propagation distances *z*. Examples of the obtained intensity and phase patterns are presented in Fig. 13.3. The OV core positions are extracted from the calculated patterns in two mutually complementary ways: as the amplitude zeros (Fig. 13.3 (a, b)) and as points with indeterminate phase, where different contours of constant phase converge [15, 19] (Fig. 13.3 (c)). To enhance the visibility of the amplitude zeros, the calculated intensity distribution $I(x, y) = |u(x, y)|^2$ (Fig. 13.3 (a)) can be transformed according to the formula

$$I(x, y) \rightarrow I_t(x, y) = \left[|u(x, y)|^2\right]^{1/n}, \quad (13.5)$$

where *n* is a large enough positive integer, normally chosen $n = 15$. In addition to (or instead of) the transformation (13.5), the numerically calculated near-zero intensity distribution was approximated by a second-degree polynomial in *x* and *y*, and the OV-core position was identified as the center of the equal-intensity ellipses for this distribution (similarly to the interpolation procedure used for the experimental data interpretation, see Section 13.2).
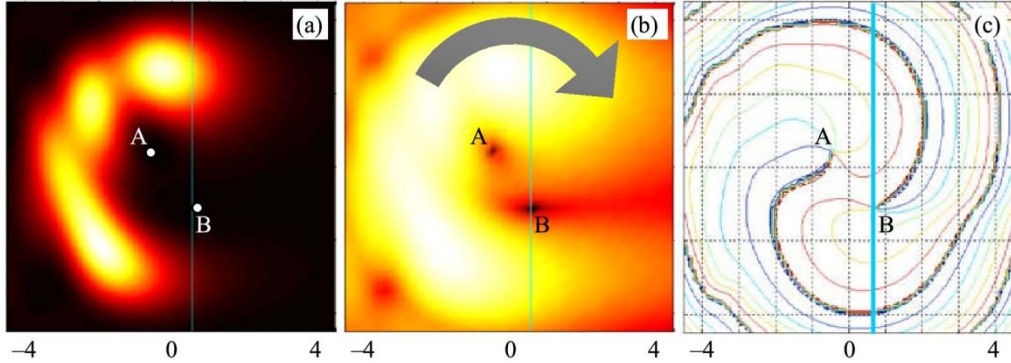
Fig. 13.3. Pseudo-color maps of the (a) intensity distribution $I(x, y)$, (b) transformed intensity distribution (13.5) with enhanced visibility of the amplitude zeros ($n = 15$) and (c) contours of constant phase (phase increment between adjacent contours is 1 rad). The images represent the profile of the diffracted beam with $m = -2$ at a distance 30 cm behind the obstacle, the screen edge is positioned at $a = 0.6b$; A and B mark the OV cores. All transverse scales are in units of *b* (13.3), the vertical cyan line is the screen edge projection, and the gray curved arrow shows the energy circulation in the incident OV beam.

In the phase maps (Fig. 13.3 (c)) the OV cores are situated at the ends of cuts (curvilinear 'bundles' of lines of different colors 'tightly touching' each other); along these cuts the phase experiences $\pm\pi$ 'jumps'.

13.3.2. Description of the Incident OV Beams

Now let us specify more rigorously the incident OV beams whose diffraction is studied numerically. Addressing the experimental situation of Section 13.2 [22, 23], we will consider the case where the incident OV beam is described by the Kummer beam model [34] which is typical when an OV beam is formed from an initial Gaussian beam with the help of a VG element (see Fig. 13.1 (c)). In this case, the input complex amplitude distribution is $u_a(x_a, y_a) = u^K(x_a, y_a, z_h)$ where

$$u^K(x_a, y_a, z_h) = \frac{z_{he}}{z_h}\sqrt{\frac{\pi}{2}}(-i)^{|m|+1}\exp\left[\frac{ik}{2z_h}(x_a^2 + y_a^2) + im\phi_a\right]$$

$$\times \frac{z_R}{z_{he} - iz_R} e^{-A} \sqrt{A} \left[I_{\frac{|m|-1}{2}}(A) - I_{\frac{|m|+1}{2}}(A) \right], \tag{13.6}$$

where $\phi_a = \arctan(y_a/x_a)$ is the azimuth (polar angle) in the screen plane, m is the OV topological charge (corresponds to the phase increment $2m\pi$ upon the round trip near the beam axis), I_ν denotes the modified Bessel function [36];

$$A = \frac{1}{4} \frac{z_R}{z_{he} - iz_R} \left[\frac{k}{z_{he}} \left(x_{ae}^2 + y_{ae}^2 \right) \right], \quad z_R = kb^2, \tag{13.7}$$

$$z_{he} = \frac{z_h}{1 + z_h/R}, \quad x_{ae} = x_a \frac{z_{he}}{z_h}, \quad y_{ae} = y_a \frac{z_{he}}{z_h}, \tag{13.8}$$

b being the Gaussian beam radius at the VG plane, see Fig. 13.1 (c) and Eq. (13.3). Eqs. (13.6)–(13.8) admit the non-planar wavefront of the initial Gaussian beam, R is the wavefront curvature radius; equation for z_R in (13.7) just formally coincides with the Raleigh range definition [2] because for finite R, the quantity b is no longer associated with the beam waist.

Another beam type is the standard LG beam, which is more suitable in theoretical analysis; here, for simplicity, we restrict our consideration by the modes with zero radial index. In many situations, the LG beam model is considered universal and is used for approximate description of more complicated circular OV beams occurring in practice. In this case $u_a(x_a, y_a) = u^{LG}(x_a, y_a, z_c)$ where [2, 4, 5]

$$u^{LG}(x_a, y_a, z_c) = \frac{(-i)^{|m|+1}}{\sqrt{|m|!}} \left(\frac{z_{Rc}}{z_c - iz_{Rc}} \right)^{|m|+1} \left(\frac{x_a + i\sigma y_a}{b_0} \right)^{|m|} \exp\left(\frac{ik}{2} \frac{x_a^2 + y_a^2}{z_c - iz_{Rc}} \right), \tag{13.9}$$

where $\sigma = \mathrm{sgn}(m) = \pm 1$, b_0 is the Gaussian envelope waist radius, z_c is the distance from the waist cross section to the screen plane (see Fig. 13.1 (b)), and $z_{Rc} = kb_0^2$ is the corresponding Rayleigh length (13.1); the current beam radius b_c and wavefront curvature radius R_c in the screen plane are determined by the known expressions

$$b_c^2 = b_0^2 \left(1 + \frac{z_c^2}{z_{Rc}^2} \right), \quad R_c = z_c + \frac{z_{Rc}^2}{z_c}. \tag{13.10}$$

Substituting (13.6) and (13.9) into (13.4) one can find the diffracted beam characteristics for arbitrary propagation distance z and arbitrary screen edge position a. This enables further determining the OV positions numerically as was described in Section 13.2, Fig. 13.3, and some examples are presented in Figs. 13.4–13.6. However, for beams (13.6)

and (13.9), the approximate analytical description of the diffracted beam structure is possible, which is considered in Section 13.4.

13.3.3. Migration of Singularities in the Diffracted OV Beams: Experimental Data Compared with Theory

The main results relating the OV positions and their behavior with varying incident beam screening (a-dependent evolution) are illustrated in Figs. 13.4–13.6. Each image shows the a-dependent migration of the OV cores over the fixed cross section of the diffracted beam for the incident Kummer beam with parameters (13.3) and $z_h = 11$ cm. In all cases, the transverse energy circulation is clockwise (see Fig. 13.3 (b)), and the OV cores describe spiral-like trajectories with opposite, counter-clockwise motion as is indicated by arrows. In compliance with the previous reports [7, 8, 19], as the screening grows (a diminishes to zero, and further down to negative values), the OVs move into the shadow region $x > a$ and eventually vanish (annihilate).
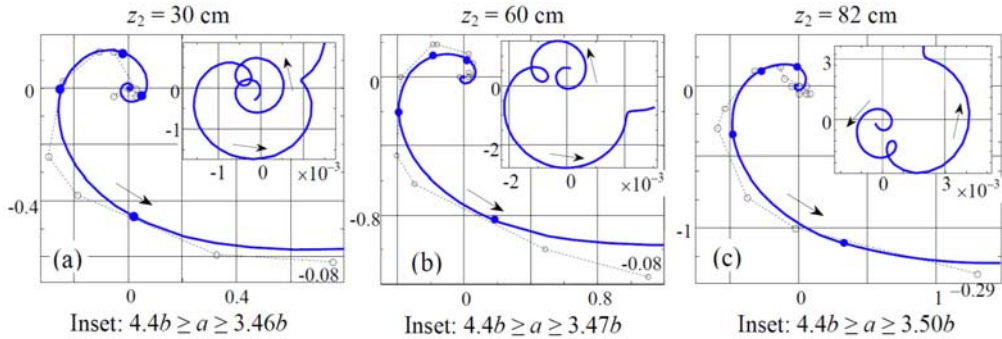
Fig. 13.4. Theoretical (solid) and experimental (dashed) trajectories of the OV cores within the cross sections of the diffracted Kummer beams with topological charge $m = -1$ (handedness of the energy circulation is as in Fig. 13.3 (b)); the cross section distance behind the obstacle is indicated above the images. All the transverse coordinates and the screen edge position a are given in units of the initial Gaussian beam radius b (13.3) at the VG plane. Arrows show the OV motion when the screen edge approaches the z-axis ($4.4b \geq a \geq 0.25b$, see Fig. 13.1 (a)). Filled circles mark the trajectories' points corresponding to decreasing half-integer $a/b = 2.0, 1.5, 1.0, 0.5$. Final positions of the screen edge where the experimental OVs apparently disappear (cannot be reliably identified) are indicated near the trajectories' ends. The insets show initial segments of the trajectories (for a within the ranges indicated below the images) that cannot be resolved in the main curves.

The detailed analysis and interpretation of these results will be performed in further sections of this Chapter; now we only comment on some general qualitative features of the OV behavior. First to note, Figs. 13.5 and 13.6 confirm earlier observations [14, 15, 19] that even very weak diffraction perturbation, when the screen edge merely 'touches' the far beam periphery and the diffraction practically does not affect the visible beam profile (which obviously takes place, for example, when $a > 4b$, cf. also Fig. 13.14 (a) below), is sufficient for the decomposition of an initial m-charged OV into a set of $|m|$ single-charged ones – the singular skeleton is really formed. Each singularity regularly

evolves with the diffracted beam propagation (growth of z) forming the OV filament [6]. Different individual filaments are marked by different colors: blue and red in case $|m| = 2$ (Fig. 13.5), and blue, red and green for $|m| = 3$ (Fig. 13.6).
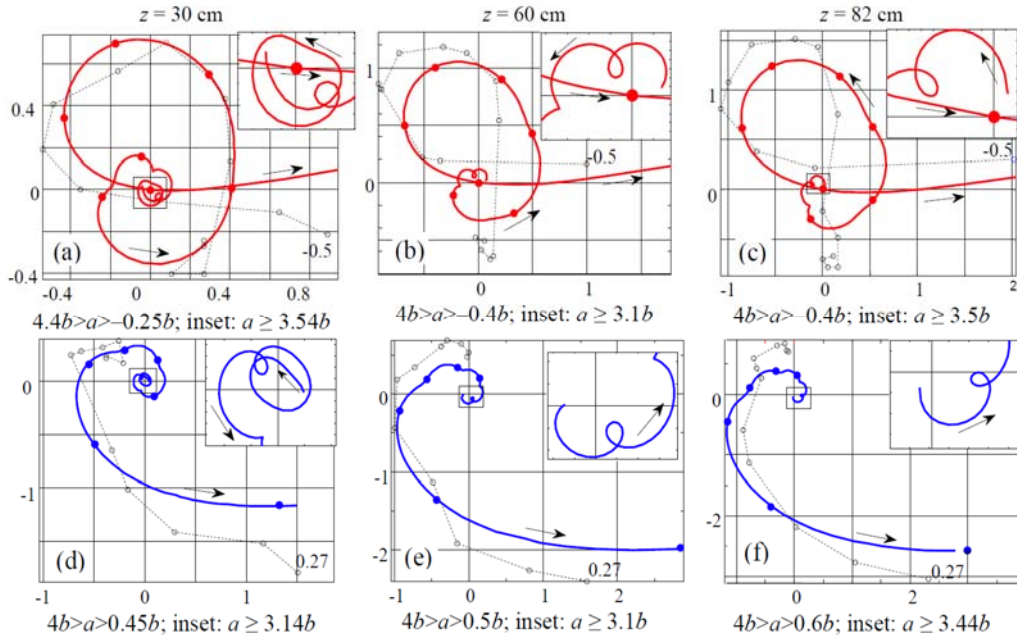
Fig. 13.5. Theoretical (solid colored) and experimental (dashed black) trajectories of the OV cores within the cross sections of the diffracted Kummer beams with topological charge $m = -2$ (handedness of the energy circulation is as in Fig. 13.3 (b)); the cross section distance behind the obstacle is indicated above each column. All the transverse coordinates and the screen edge position a are given in units of the initial Gaussian beam radius b (13.3) at the VG plane. Arrows show the OV motion when the screen edge approaches the z-axis (see Fig. 13.1 (a)); the range of the screen edge positions a accepted for calculations is indicated below each image. Filled circles mark the trajectories' points at which a/b accepts decreasing half-integer values starting from $a/b = 3.0$. The initial experimental points correspond to $a/b = 4.0$, final positions of the screen edge where the OVs could not be reliably identified are indicated near the final experimental points. The insets show magnified initial segments of the trajectories (marked by the rectangles), corresponding ranges of a are indicated below the images.

Neither in experiment nor by the numerical study could we detect the initial 'moment' (the value of a) at which the central OV of the multicharged incident beam starts to 'split'; likewise, we could not trace the earliest stages of the single-charged OV displacement from the axis z in case of the first-order beam diffraction (Fig. 13.4). With growing a (the screening weakens), the spirals of the OV trajectories seem to make infinite number of rotations around the axis z, gradually approaching the origin $x = y = 0$. For this reason, the initial points of all the trajectories correspond to certain finite OV displacement, after which its behavior becomes more regular and can be reliably traced both numerically and in the experiment.
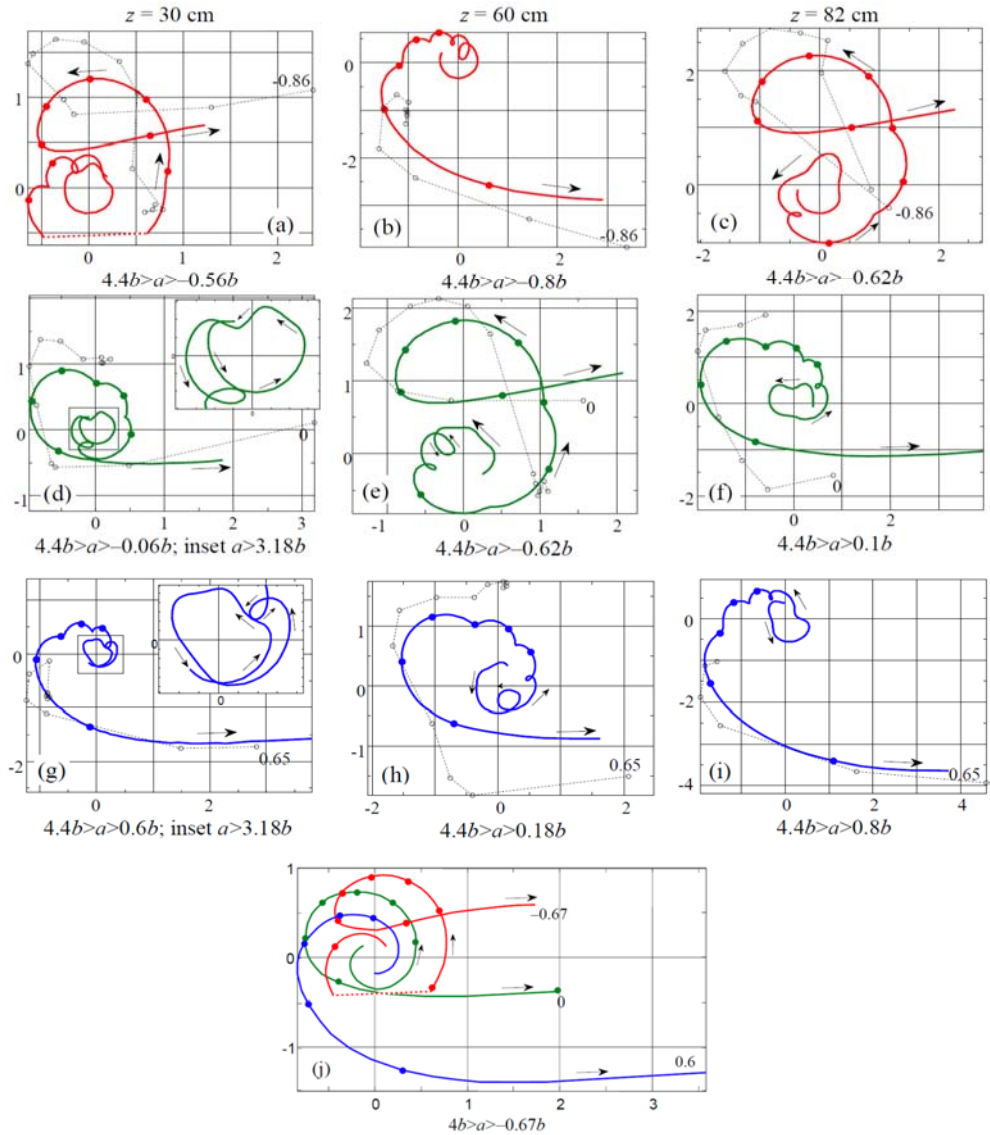
Arrows show the OV motion when the screen edge approaches the *z*-axis (see Fig. 13.1 (a)); the range of the screen edge positions *a* assumed for calculations is indicated below each image. Filled circles mark the trajectories' points at which *a/b* accepts decreasing half-integer values starting from *a/b* = 3.0. The insets in (d) and (g) show magnified initial segments of the trajectories (marked by the rectangles), corresponding ranges of *a* are indicated below the images.

Fig. 13.6. (a)–(i) Theoretical (solid colored) and experimental (dashed black) trajectories of the OV cores within the cross sections of the diffracted Kummer beams, the cross section distance behind the obstacle is indicated above each column; (j) theoretical trajectories of the OV cores in the diffracted LG beam (13.9), (13.10) with parameters (13.11) for the distance behind the obstacle *z* = 30 cm. The topological charge of the incident OV is *m* = –3, all the transverse coordinates and the screen edge position *a* are given in units of *b* (13.3) or (13.11). The initial experimental points correspond to *a/b* = 2.2, final positions of the screen edge where the OVs could not be reliably identified are indicated near the final experimental points.

355

A good quantitative agreement between the experimental results and the simulation can be detected only for a single-charged OV (Fig. 13.4) whereas for two- or three-charged OVs just a qualitative correspondence is seen (see Figs. 13.5 and 13.6). This can be associated with the special character of the VG used in the experiment: With increasing order of the OV beams generated by the 'fork' hologram, the beams' inclination with respect to the initial Gaussian beam axis also grows, which invokes the OV beam deformation [35] so that at the screen plane, the incident OV beam partly loses its symmetry, and a set of secondary OVs already exists instead of a single multicharged OV expected theoretically. Actually, Figs. 13.5 and 13.6 show that discrepancies between the experimental and theoretical trajectories grow with $|m|$.

Another reason for this is that the spiral-like OV evolution is complicated by multiple fine details distinctly seen in the theoretical curves in Figs. 13.4–13.6: the spirals experience oscillatory pulsations, sometimes resulting in trajectory self-crossings, regions of retrograde azimuthal motion (loops), etc. (further we will show that this is a characteristic feature of the Kummer beam diffraction, see Section 13.4). These fine details are the most articulate under the WDP conditions ($a \gg b$) but with decreasing a they disappear and the spirals become more regular. Presence of the fine details makes the experimental detection of the current OV positions difficult, as is the case of Figs. 13.5 and 13.6. In case of Fig. 13.4, these details only exist for very small radial deviation of the OV from the nominal beam axis (~0.001b, see the insets in Figs. 13.4 (a–c)), and the observable part of the OV trajectory is already a regular spiral favorable for the experimental observations. Note that for $|m| = 2$ (Fig. 13.5) one of the OV trajectories always intersects the point $x = y = 0$, which confirms the earlier suggestion that when an even-charged circular OV beam diffracts on a sharp edge positioned at $a = 0$, one of the diffracted beam OVs is fixed at the incident beam axis [19].

An interesting peculiar feature is seen in Fig. 13.6 (a). For certain conditions, the OV trajectory experiences a discontinuity denoted by the dashed straight-line segment: a minute advance of the screen edge induces an articulate 'jump' of the OV core to a remote point of the diffracted beam cross section. This situation is rather typical and will be a subject of special consideration in Sections 13.6 and 13.7.

For comparison, the OV migration in the diffracted LG beam (13.9) is illustrated in Fig. 13.6 (j) for conditions corresponding to Figs. 13.6 (a, d, g) ($z = 30$ cm, $m = -3$). Numerical values of the LG beam parameters are chosen so that the transverse profile of the incident LG beam at the screen plane be in maximal possible similarity to the Kummer beam spatial profile of [20, 21]. This non-rigorous requirement is satisfied if we accept in Eqs. (13.9) and (13.10)

$$b_c = b = 0.232 \text{ mm}, \; R_c = 57 \text{ cm}, \; b_0 = 0.17 \text{ mm}, \; z_{Rc} = 28.5 \text{ cm}, \; z_c = 27 \text{ cm}. \quad (13.11)$$

The general pattern of the OV trajectories in Fig. 13.6 (j) looks qualitatively similar to that of the Kummer beam diffraction; even the discontinuity of the 'red' trajectory is confirmed. At the same time, the OV trajectories in the diffracted LG beam are much smoother and contain no radial pulsations, nor small-scale self-crossings ('loops').

13.4. Mathematical Model of the Singular Skeleton Evolution in Diffracted OV Beams

13.4.1. Asymptotic Analytical Model

If the incident beam is an LG beam, the integral (13.4) can, in principle, be evaluated analytically but when $|m| > 1$, the explicit representation is cumbersome and physically obscure [11, 12]; for the incident Kummer beams, an exact analytical representation is unknown. Nevertheless, the situation can be examined analytically by means of the simple model which is derived for $a \gg b$ (WDP case) but appears to be practically valid when the screen edge is separated by several b from the incident beam axis [21] (see Fig. 13.1). In this approximation, the diffracted beam (13.4) can be considered as a superposition of the unperturbed incident beam and the edge wave 'emitted' by the screen edge [2]. For any circular OV beam considered in this Chapter, near the z-axis its complex amplitude distribution can be presented in the form

$$E_{\text{inc}} = B_0 \left(\frac{r}{b} \right)^{|m|} \exp(im\phi) \exp(ikz), \tag{13.12}$$

where $r = \sqrt{x^2 + y^2}$ and $\phi = \arctan(y/x)$ are the polar coordinates in the observation plane. The quantity B_0 is a complex constant depending on the propagation distance and the beam type (e.g., Kummer or LG), as well as on its specific parameters, which can easily be derived from the explicit expressions (13.6) or (13.9). Near the origin of the observation plane, the edge-wave amplitude approximately amounts to

$$E_{\text{edge}} = D_0(a,z) \exp\left[ik \left(z + \frac{a^2}{2z} - x\frac{a}{z} \right) \right]$$

$$= D_0(a,z) \exp\left[ik \left(z + \frac{a^2}{2z} - r\frac{a}{z}\cos\phi \right) \right], \tag{13.13}$$

with the complex coefficient $D_0(a,z)$ decreasing with growing $|a|$ and z. Eq. (13.13) differs from the similar expression used in Ref. [21] by the x-proportional term responsible for the wavefront inclination in the (xz) plane (see Fig. 13.1). The positions of the OV cores are determined by the condition $E_{\text{edge}} + E_{\text{inc}} = 0$, which entails

$$\frac{r}{b} = \left[\frac{|D_0(a,z)|}{|B_0|} \right]^{1/|m|}, \tag{13.14}$$

$$\phi + M\cos\phi = C_{N+1} + k\frac{a^2}{2mz}, \tag{13.15}$$

357

where

$$M = \frac{kra}{mz}, \tag{13.16}$$

and the coordinate-independent term C_{N+1} possesses its own value for each secondary OV numbered by $N = 0, 1, \dots |m| - 1$,

$$C_{N+1} = \frac{1}{m} \left[\arg D_0(a, z) - \arg B_0 + (2N - 1)\pi \right]. \tag{13.17}$$

Despite their very approximate character, Eqs. (13.14) and (13.15) enable efficient qualitative analysis of the OV trajectories. First, one observes that under the WDP conditions, the OV off-axis displacement $r \rightarrow 0$, and the second summand in the left-hand side of (13.15) can be neglected ($M \rightarrow 0$). Then Eq. (13.15), in full agreement with the experiment [20], predicts the monotonous behavior of the OV azimuth upon monotonous variation of a or z. Together with the monotonous nature of $D_0(a, z)$ in Eq. (13.14), this dictates the spiral character of the OV trajectory, which (theoretically) makes infinite number of rotations near the z-axis while $a \rightarrow \infty$ (the focus-type singularity [16]). Also, Eq. (13.15) with $M \rightarrow 0$ makes it obvious that the rate of the OV spiral evolution should slow down with a decrease of a and an increase of z, which is also confirmed by experiments and numerical calculations [20, 21].

13.4.2. Refined Analytical Model

This procedure can be substantiated and refined by employing the asymptotic representation of the diffracted beam field [21]. To this purpose, we resort to the asymptotic expression for the diffracted beam amplitude (13.4) derived in Appendix:

$$u(x, y, z) \simeq B_1 \left(\frac{r}{b} \right)^{|m|} \exp(im\phi)$$

$$- \frac{D_1}{a^3} \exp\left[\frac{ika^2}{2} \left(\frac{1}{z_h} + \frac{1}{z} \right) - \frac{ika}{z} x \right] + \frac{D_2}{a} \exp\left[\frac{ika^2}{2} \left(\frac{1}{z_d} + \frac{1}{z} \right) - \frac{ika}{z} x \right], \tag{13.18}$$

where z_d is defined in Eq. (13.A17),

$$B_1 = \sqrt{\frac{\pi}{2^{3|m|}}} \left(\frac{-iz_e}{z + z_h} \right)^{|m|+1} \frac{z_R^{|m|+1}}{z_e^{|m|/2} (z_e - iz_R)^{|m|/2+1}}, \tag{13.19}$$

$$D_1 = |m|(-i)^{|m|+1} \sqrt{\frac{i}{2\pi}} \frac{z_h}{z} \left[k \left(\frac{1}{z_h} + \frac{1}{z} \right) \right]^{-3/2}, \tag{13.20}$$

$$D_2 = -\frac{ik}{2^{2|m|}} \sqrt{\frac{i}{2\pi}} \frac{z_{he}}{z\,z_h} \frac{z_R^{2|m|+1}}{z_{he}^{|m|} \left(z_{he} - iz_R\right)^{|m|+1}} \left[k\left(\frac{1}{z_d} + \frac{1}{z}\right)\right]^{-3/2}. \tag{13.21}$$

Equations (13.18)–(13.21) are valid if $a >> b$ and only near the axis, $x << b$, $y << b$ (see Eq. (13.A4)) but they express the physical essence of the diffraction process [2]. The first term of Eq. (13.18) describes the unperturbed incident beam and is an analogue of Eq. (13.12), while the role of the screen is accumulated in the second and third terms that describe a sort of 'edge wave' (13.13) which interferes with the incident beam, thereby forming the diffraction pattern.

As a result, for the diffraction of the Kummer beam (13.6)–(13.8), instead of the simple relations (13.14), (13.15), the OV polar coordinates can be determined via equations

$$\frac{r}{b} = \left[\left|\frac{D_1}{a^3}\exp\left(\frac{ika^2}{2z_h}\right) - \frac{D_2}{a}\exp\left(\frac{ika^2}{2z_d}\right)\right| \cdot \frac{1}{|B_1|}\right]^{1/|m|}, \tag{13.22}$$

$$\phi + M\cos\phi = \frac{1}{m}\arg\left[\frac{D_1}{a^3}\exp\left(\frac{ika^2}{2z_h}\right) - \frac{D_2}{a}\exp\left(\frac{ika^2}{2z_d}\right)\right] + \frac{ka^2}{2mz} - \frac{1}{m}\arg B_1 + \frac{2N}{m}\pi, \tag{13.23}$$

where M is defined by (13.16).

Quite similarly, based on Eqs. (13.A1), (13.A8) and (13.A9), the analogs of Eqs. (13.18)–(13.21) for the LG beam (13.9), (13.10) for large enough $a >> b_c$ can be derived:

$$u(x,y,z) \simeq Br^{|m|}\exp(im\phi) - Da^{|m|-1}\exp\left[\frac{ika^2}{2}\left(\frac{1}{z_c - iz_{Rc}} + \frac{1}{z}\right)\right], \tag{13.24}$$

where

$$B = \frac{1}{\left(z + z_c - iz_{Rc}\right)^{|m|+1}}, \quad D = \sqrt{\frac{i}{2\pi}}\frac{k}{z}\left(z_c - iz_{Rc}\right)^{-|m|-1}\left[k\left(\frac{1}{z} + \frac{1}{z_c - iz_{Rc}}\right)\right]^{-3/2}. \tag{13.25}$$

Hence, again, the explicit expressions for the OV cores' polar coordinates can be easily found by equating (13.24) to zero:

$$r = \left[a^{|m|-1}\exp\left(-\frac{a^2}{2b_c^2}\right)\left|\frac{D}{B}\right|\right]^{1/|m|}, \tag{13.26}$$

$$\phi + M\cos\phi = \frac{1}{m}\left[\arg D - \arg B\right] + \frac{ka^2}{2mz} + \frac{ka^2}{2mR_c} + \frac{2N}{m}\pi. \tag{13.27}$$

The quality and descriptive abilities of the described asymptotic model are illustrated in Fig. 13.7 where, for simplicity, the OV azimuths are calculated discarding the cosine terms in Eqs. (13.23) and (13.27). The most noticeable model limitation is that it describes all the secondary OVs by the same equations differing only by N thus predicting that their radial coordinates are identical and the azimuthal ones differ only by additive constants (in the case of Fig. 13.7 with $|m| = 3$ this additive constant defining the azimuthal 'distance' between different OV positions is $2\pi/3$). Nevertheless, one can see that the approximate solutions (13.22), (13.23) and (13.26), (13.27) fairly reflect main qualitative features of the a-dependent OV evolution in the diffracted beam cross sections: the dashed curve in Fig. 13.7 (a) explicitly shows the radial pulsations of the spiral trajectory (cf. Figs. 13.5 and 13.6); moreover, the dashed curves in Fig. 13.7 (b) contain segments where ϕ decreases with growing a explaining the retrograde evolution of the spirals and formation of the loops well seen in almost all images of Figs. 13.4–13.6. In fact, Eqs. (13.22) and (13.23), to a certain degree, disclose the physical reason for the radial pulsations and loops that are characteristic for all images of Figs. 13.5 and 13.6 except Fig. 13.6 (j): these are consequences of the interference between the two summands in brackets of the right-hand sides of these equations. In turn, these interfering terms appear due to the oscillatory behavior of the Kummer beam amplitude ('ripple structure') [34] and the slow amplitude decay for large transverse radius $r_a \to \infty$, so that the edge wave represented by the second line of Eq. (13.18) is formed as a superposition of contributions originating from different points of the screen edge with different amplitudes and initial phases that non-monotonously depend on a and/or z. With increasing z_h in Fig. 13.1 (c) and Eqs. (13.6)–(13.8), oscillations of the amplitude and phase at the Kummer beams' periphery are gradually mitigated, and the pulsations of the OV trajectories in corresponding diffracted beams are softened and eventually disappear (this is not shown in figures but was confirmed by numerical calculations). The same reasoning perfectly explains the 'smooth' OV trajectories in the diffracted LG beams (Figs. 13.6 (j), 13.7 (c), 13.7 (d)) where the amplitude decays monotonously and very rapidly for $r_a \to \infty$.

Thus providing a good qualitative basis of the OV trajectories' behavior for diffracted Kummer beams, the asymptotic model gives but a rather poor quantitative agreement with accurate numerical data, and even this poor agreement is only observed at large enough $a \gtrsim 3b$. In contrast, upon diffraction of LG beams, the good quantitative approximation for at least one of the OVs is realized up to $a \approx b$ (Fig. 13.7 (c)). This is rather surprising in view of the asymptotic character of the model that was derived assuming $a \gg b$. As to the azimuthal OV positions (Fig. 13.7 (d)), the main peculiarity of the model (dashed) curves is their perfectly smooth character in contrast to the accurate numerical data that demonstrate segments of relatively slow and rapid growth of ϕ. The 'steep' segments of the solid curves near the points where $\phi = -\pi/2, 3\pi/2, 7\pi/2$ (clearly seen in Fig. 13.7 (d) but masked by additional details in Fig. 13.7 (b)) as well as the jumps of the red curves near $a/b = 2.35$ in Fig. 13.7 (b) and $a/b = 2.6$ (corresponding to the discontinuities in Figs. 13.6 (a) and 13.6 (j)) in Fig. 13.7 (d) are associated with the discarded cosine terms in (13.23) and (13.27). The nature of these peculiarities will be discussed below in Section 13.6.
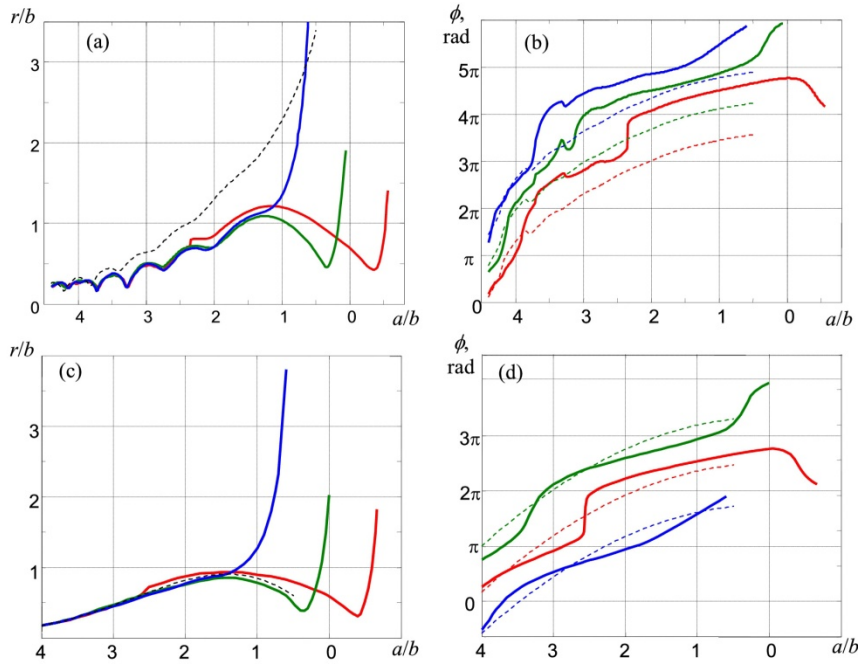
Fig. 13.7. Radial and angular polar coordinates of the OV cores in the diffracted OV beam with topological charge $m = -3$, cross section $z = 30$ cm. (a, b) Incident Kummer beam; (c, d) incident LG beam. Solid curves illustrate the numerically calculated evolution of r and ϕ when the screen edge moves from large positive x towards the beam axis and slightly further; inverse horizontal scale indicates the screen edge position a in units of b (13.2) or (13.11). Curves of different colors describe different secondary OVs (curves of the same colors in (a, b) and in Fig. 13.6 (b, e, i) describe the same OVs); thin dashed curves represent the asymptotic approximation of (a, b) (13.22), (13.23) and (c, d) (13.26), (13.27) with $M = 0$.

13.5. Theoretical Study of the OV Migration: LG Beams

The first experimental observations that have stimulated this research and have been described in Section 2 dealt with the Kummer beams. However, some general features of OV diffraction can more easily be understood with the help of simpler examples of LG incident beams (Fig. 13.1 (b)). In this section we analyze the OV localization and migration in case of diffraction of the simplest low-order OV beams, mostly under the WDP conditions which enable efficient and insightful interpretation based on the asymptotic analytical model described above. In particular, in this case the OV displacement from the z-axis is supposed to be small, due to which $M \ll 1$, and the cosine terms in the left-hand sides of Eqs. (13.23), (13.27) can be discarded. The WDP requirements impose natural limitations on the range of possible variations of the screen edge position a; that is why in this section we mainly consider the z-dependent evolution of the diffracted beams for several fixed a. As everywhere in this Chapter, the transverse geometrical parameters are expressed in units of the incident beam transverse scale. For LG beams, this scale is represented by b_c (13.10). In order to preserve geometrical

361

conditions of Section 13.2 and for determinacy of numerical examples, we chose b_c to be equal to the Kummer beam transverse scale (13.3), i.e. in all further calculations we suppose

$$k = 10^5 \text{ cm}^{-1} \quad \text{and} \quad b_c = 0.232 \text{ mm.} \tag{13.28}$$

13.5.1. OV Displacements: Incident Beam with Plane Wavefront

Following [14, 15, 19], we start with analyzing the single-charged incident LG beam ($m = -1$) with its waist at the screen plane, i.e. in equations (13.9) and (13.10)

$$z_c = 0, \quad b_c = b_0, \quad R_c = \infty, \tag{13.29}$$

which means

$$z_{Rc} = 53.8 \text{ cm.} \tag{13.30}$$

For a single-charged OV beam, the main consequence of the WDP is the OV displacement from its nominal position at the beam axis $x = 0$, $y = 0$. The main results relating the positions of the OV cores in the diffracted beam cross-section at different distances z behind the screen plane are given in Fig. 13.8 for four fixed screen-edge locations (see Fig. 13.1 (a)): $a = 3b_c$, $a = 2b_c$, $a = b_c$, and $a = 0.6b_c$. In order to divert from the trivial component of the OV migration associated with the beam divergence, the transverse OV coordinates are normalized by the current beam radius

$$b_d = b_0 \sqrt{1 + \frac{z^2}{z_{Rc}^2}} \, . \tag{13.31}$$

As expected, the distinct spiral-like trajectories are only observed under conditions of weak OV-beam perturbation ($a = 3b_c$ and $a = 2b_c$); the trajectories for $a = b_c$ and $a = 0.6b_c$ are given for comparison. Actually, these curves also contain certain spiral-like segments corresponding to the very small propagation distances, which are hardly available both to analysis and to observation because of the diffraction-fringes effects. On the other hand, under the WDP conditions, the OV displacement from the incident beam axis is rather small. This is noticeable, e.g., in Fig. 13.4 for the a-dependent evolution in the diffracted Kummer beam and is clearly seen in Fig. 13.8 (a) by matching the blue spiral for $a = 2b_c$ against the red and black curves for $a = b_c$, and $a = 0.6b_c$; in case of $a = 3b_c$ the spiral is so small that it is separately magnified in Fig. 13.8(b).

The images of Fig. 13.8 are actually transverse projections of the 3D OV filaments that evolve within the "body" of the propagating diffracted beam. Such 3D spirals for $a = 2b_c$ and $a = 3b_c$ are illustrated by Fig. 13.9. Here the longitudinal coordinate z varies within the range

$$10 \text{ cm} = 0.186 z_{Rc} < z < 600 \text{ cm} \approx 11.15 z_{Rc}.$$
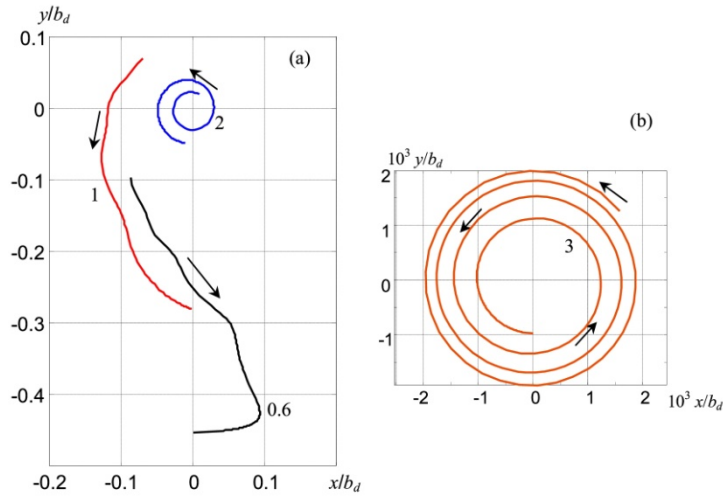
Fig. 13.8. *z*-Dependent evolution of the OV core position in the cross section of the diffracted LG beam of equations (13.9), (13.10), (13.29) with $m = -1$ and $R_c = \infty$ for (a) $a = 2b_c$ (blue), $a = b_c$ (red), $a = 0.6b_c$ (black) and (b) $a = 3b_c$ (brown); each curve is marked by the corresponding value of a in units of b_c. Arrows indicate directions of the OV motion, initial points of the curves correspond to $z = 10$ cm $= 0.186z_{Rc}$ (near field), and final points correspond to $z = \infty$ (far field).

Note that the 'motion' of the OV core along its trajectory is not uniform: practically the entire observable evolution happens for the first 10 % of the full range of z variation (cf. Fig. 13.10 below). To present the 3D trajectories more conveniently, in Figs. 13.9 (a), 13.9 (b) the longitudinal scales are non-uniform: the real distance z is normalized by the scale factor (13.31). Remarkably, even with this precaution, the region $z < 10$ cm cannot be shown properly because with decreasing z, the rate of the spiral rotation (theoretically) infinitely grows while the spiral pitch (distance between consecutive coils) infinitely decreases. This is supported by the simplified asymptotic model (13.12)–(13.15) and (13.24)–(13.27) which at WDP conditions ($M \ll 1$) leads to the approximate rule

$$\phi \approx \text{const} + k\frac{a^2}{2mz}. \tag{13.32}$$

Obviously, with increasing z, the rotation practically stops whereas for small z the rate of rotation $d\phi/dz$ can be rather high. However, this implies no unphysical divergence for very small z because when $z \to 0$, the relation $D \to 0$ also takes place (see (13.25)) and Eqs. (13.14) and (13.24) dictate that with growing rate of rotation, the OV off-axial displacement becomes so small that the "theoretic" spiral motion is practically imperceptible.

Importantly, for $z \to \infty$ all the OV trajectories in Fig. 13.8 approach the vertical axis. This fact was noticed previously and interpreted based on the general concept that the diffracted beam intensity distribution rotates during propagation [9, 13, 19] (cf. Fig. 13.2). Just after the screen, the diffracted beam intensity distribution loses circular symmetry but preserves

363

the mirror symmetry with respect to an axis orthogonal to the screen edge. In the course of further propagation, the beam shape continuously changes, generally, in a rather complicated way. But this transformation possesses a sort of regular rotational component, which, in the far field, results in an intensity distribution with another symmetry axis, orthogonal to the initial one and parallel to the screen edge. Accordingly, in the far field, the OV of the diffracted beam eventually approach this symmetry axis that in normalized coordinates of Fig. 13.8 coincides with the y-axis.
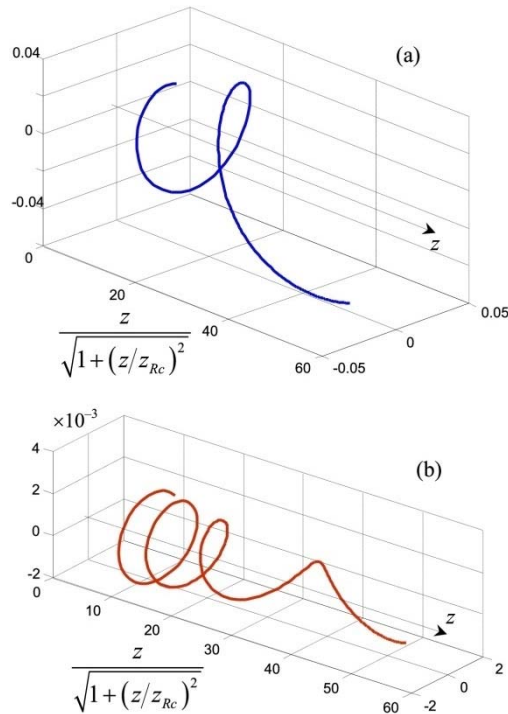
Fig. 13.9. 3D evolution of the OV core positions in the diffracted LG beam (13.9), (13.10), (13.29) with $m=-1$ and $R_c = \infty$ for (a) $a = 2b_c$ and (b) $a = 3b_c$; transverse coordinates are in units of b_d (13.31). The blue and brown spirals in Fig. 13.8 represent projections of these trajectories viewed against axis z.

13.5.2. OV Displacements: Incident Beam with Spherical Wavefront

The last conclusion of the previous section was drawn from the OV diffraction analysis based on an assumption that the wavefront of the incident OV beam is plane. Now consider what influence can be caused by the wavefront curvature. Of course, this can be carried out by calculating the diffraction integral (13.4) with the input amplitude distribution (13.9), (13.10) corresponding to a non-planar wavefront, or with the help of the model equations (13.25)–(13.27) with the necessary value of R_c but it would be suitable to involve another simple rule for transformation of the diffracted beam complex amplitude that occurs if the incident beam is modified according to the equation

$$u(x_a, y_a) \rightarrow u(x_a, y_a) \exp\left(ik \frac{x_a^2 + y_a^2}{2R_c} \right), \tag{13.33}$$

(e.g., the plane front is replaced by the spherical one with the same intensity profile) [14]. In this situation, if the initial distribution $u(x_a, y_a)$ produces a diffracted beam with complex amplitude $u(x, y, z)$, the modified initial beam (13.33) produces the diffracted beam distribution

$$u_e(x, y, z) = \frac{1}{1 + \dfrac{z}{R_c}} \exp\left[ik \frac{x^2 + y^2}{2(z + R_c)} \right] u\left(\frac{x}{1 + z/R_c}, \frac{y}{1 + z/R_c}, \frac{z}{1 + z/R_c} \right). \tag{13.34}$$

To elucidate the meaning of this rule, let us suppose that the incident beam $u(x_a, y_a)$ possesses a plane wavefront, except for the helical component associated with the term $(x_a + i\sigma y_a)^{|m|}$ in Eq. (13.9). Also, we suppose that this beam ('prototype beam'), being diffracted, produces in the cross section z_0 behind the screen such complex amplitude distribution, for which the OV core is situated in the point $(x = x_0, y = y_0)$. Hence, Eq. (13.34) dictates that the modified incident beam (13.33) produces the diffracted beam in whose cross section

$$z = \frac{z_0}{1 - z_0/R_c}, \tag{13.35}$$

the OV core is located in the point

$$x_r = \frac{x_0}{1 - z_0/R_c}, \quad y_r = \frac{y_0}{1 - z_0/R_c}. \tag{13.36}$$

In particular, the far field of the modified spherical-front beam (13.33) is realized when $z \rightarrow \infty$ which corresponds to the finite cross section of the prototype beam, $z_0 = R_c$. Note that transformation (13.36) affects only the off-axial distance of the OV position while its azimuth $\phi_r = \arctan(y_0/x_0) = \arctan(y_r/x_r)$ remains the same as in the prototype plane-front beam.

This reasoning suggests a simple procedure for determining the azimuthal far-field positions of the OV cores in the diffracted LG beam with non-planar wavefront. It requires knowledge of the OV trajectory for the prototype plane-front beam (see Fig. 13.10 where the blue spiral of Fig. 13.8 (a) is magnified and furnished with marks denoting the propagation distances behind the screen in centimeters). For example, when the incident beam wavefront possesses the curvature radius $R_c = 80$ cm, Eq. (13.35) shows that the far field for the diffracted beam is realized at $z_0 = R_c = 80$ cm. Accordingly, the corresponding

OV azimuth coincides with the azimuth of the red rectangle marked "80" in Fig. 13.10. And indeed, the independently calculated OV trajectory for the incident beam (13.9) with $R_c = 80$ cm (green curve) is oriented close to this direction, and the small discrepancy can be explained by the limited range of the propagation distances accepted for the green curve calculation (in fact, the 'genuine' far field with infinite propagation distance was never reached). The same is correct for other examples corresponding to $z_0 = R_c = 18$ cm (red curve), 30 cm (brown curve) and infinity (black curve). This reasoning distinctly shows that the far-field OV position belongs to the symmetry axis parallel to the screen edge only if the incident LG beam possesses a plane wavefront.
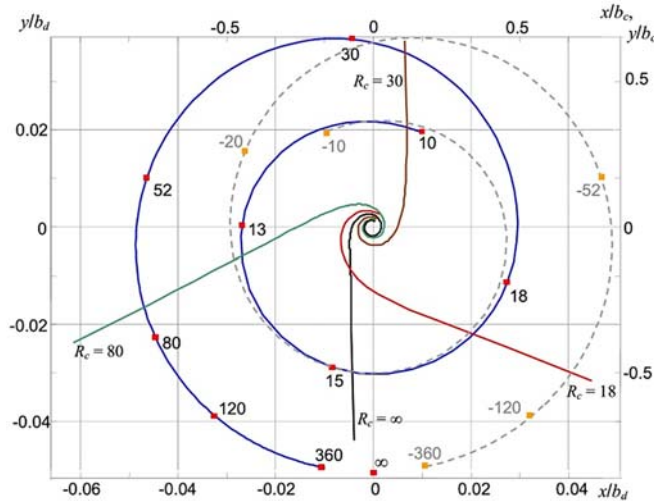
Fig. 13.10. Illustration of the far-field azimuthal OV positions in diffracted beams with non-planar wavefront for $m = -1$ and $a = 2b_c$. Blue curve is the transverse projection of the OV trajectory in the prototype plane-front diffracted beam (cf. Fig. 13.8 (a), blue curve, and Fig. 13.9 (a)), pale grey dotted curve represents its branch for the negative propagation distances. The left and bottom scales show the current OV coordinates in normalized units (13.31), red (yellow) rectangles denote the propagation distance marked in centimeters. Red, brown, green and black curves are the transverse projections of the OV trajectories in the modified spherical-front diffracted beams (13.33) (radius of curvature is indicated near each curve, the OV coordinates are measured in units of b_c, and marked in the right and top scales).

Further application of this procedure to cases with $R_c < 0$ (converging beams) requires knowledge of the plane-front diffracted beam behavior at $z_0 < 0$, which seems non-physical. However, the Fresnel–Kirchhoff integral (13.4) formally is valid for any z; moreover, equations (13.4), (13.9) and (13.10) suggest that

$$u^*\left(x_0, y_0, -z_0\right) = u\left(x_0, -y_0, z_0\right),$$

where the asterisk denotes complex conjugation. This means that positions for the amplitude zeros at negative z_0 can be easily found once they are known for positive z_0. Additionally, to get the far-field OV positions, we should take into account that in

Eq. (13.35) z tends to positive infinity, and for negative z_0 this implies that transformation (13.36) inverts the signs of both transverse coordinates. As a result, the 'prototype beam' OV trajectory for negative z_0 can be obtained by a mirror reflection of the blue spiral described above, and is presented in Fig. 13.10 as a pale grey dashed curve. This can be employed exactly in the same manner as the blue curve itself, with the help of corresponding distance marks, some of which are explicitly indicated.

Whereas for diverging beams (positive R_c), the symmetrical structure of the intensity distribution, typical for the plane-front beams, does not exist in the 'physical' range $z > 0$ (the far-field intensity pattern reproduces the prototype beam structure at finite z_0), for converging beams with $R_c < 0$ such a possibility is realized at finite z. According to Eqs. (13.35) and (13.36), this occurs when $z = -R_c > 0$, which corresponds to $z_0 = \infty$. It is expectable because the plane $z = -R_c > 0$ is actually a focal plane of the 'lens' performing transformation (13.33), and in this plane the Fraunhofer diffraction takes place which is equivalent to the far field propagation [1, 2].

The resulting azimuthal OV positions in diffracted LG beams with spherical wavefronts are illustrated in Fig. 13.11. Note that when $R_c \to \infty$, all the curves approach the azimuth values $\phi_r = (3/2)\pi$, $(7/2)\pi$ and $(15/2)\pi$, which means that the OV trajectories always end at the negative half-axis y, as was discussed above. This example also shows the advantages of the WDP conditions. Theoretically, in cases of strong beam screening, the wavefront curvature also affects the OV positions in the diffracted beam cross section but the red and black curves in Fig. 13.11 display a rather limited range of possible azimuthal deviations, and their sensitivity to the incident wavefront curvature appears to be low.
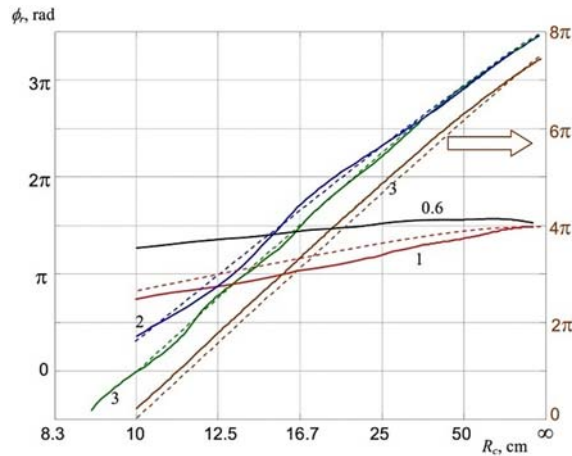
Fig. 13.11. Far-field azimuthal OV positions in the diffracted LG beam (13.9) with $m = -1$ vs. the wavefront curvature radius: (brown curve) $a = 3b_c$, right vertical scale; (blue curve) $a = 2b_c$ (cf. Fig. 13.10); (red curve) $a = b_c$ (cf. Fig. 13.8 (a)); (black curve) $a = 0.6b_c$ (cf. Fig. 13.8 (a)). The green curve represents the far-field orientation of the straight line connecting two secondary OVs in the diffracted LG beam (13.9) with $m = -2$, $a = 3b_c$ (cf. Fig. 13.13, dashed line). Each curve is marked by the corresponding value of a in units b_c; dashed lines illustrate the analytical approximations (13.37) for the solid curves of the same colors.

367

All these conclusions are based on the numerical simulations but they are also justified by the approximate model of Eqs. (13.26), (13.27). First, we note that if we introduce a finite R_c by means of transformation (13.33), the set of parameters (13.28)–(13.30) becomes modified: b_c remains the same as in Eq. (13.28) but it is no longer equal to the new waist radius b_0, and z_c is determined by the new waist position. Accordingly, the Rayleigh length of the modified LG beam $z_{Rc} = kb_0^2$ differs from the value of Eq. (13.30) but Eqs. (13.10) entail the relation

$$\frac{z_c}{z_{Rc}} = \frac{kb_c^2}{R_c} .$$

Then, with the help of Eqs. (13.25) and (13.27) with negligible M one can easily derive the far-field ($z \rightarrow \infty$) representation of the OV azimuth:

$$\phi_\infty = \frac{|m|}{m}\left(\frac{\pi}{2} - \arctan\frac{kb_c^2}{R_c}\right) + \frac{ka^2}{2mR_c} + \frac{1}{2m}\arctan\frac{kb_c^2}{R_c} + \frac{2N}{m}\pi . \qquad (13.37)$$

The corresponding dependences $\phi_\infty(R_c)$ for $m = -1$ ($N = 0$) are presented in Fig. 13.11 by the brown, blue and red dashed curves (since the azimuth values differing by a complete angle are equivalent, upon constructing the dashed curves necessary integer numbers of 2π were added to the immediate results of (13.37)). One can see that expression (13.37) provides a rather good approximation for the precise numerical data, especially for large R_c and $a = 2b_c$ and $a = 3b_c$; when the screening grows (e.g., for $a = b_c$) and the WDP conditions are violated, the approximation loses its quantitative accuracy but remains qualitatively valid.

13.5.3. Incident LG Beam with the Second-Order OV

A similar WDP-induced behavior is typical for higher-order OV beams. As an example, we consider the diffraction of a LG beam (13.9) with $m = -2$ and the same parameters (13.28)–(13.30). The main difference from the charge-1 case is that diffraction makes the incident OV decompose into two single-charged secondary OVs which evolve separately within the diffracted beam 'body'. At the WDP conditions, they form a 'double spiral' (Fig. 13.12), each component being quite similar to the OV trajectories observed in the diffracted beam with $|m| = 1$ (Fig. 13.9). Transverse projections of the trajectories shown in Fig. 13.12 are presented in more detail in Fig. 13.13; similarly to Fig. 13.10, the distance marks are added denoting the current longitudinal positions. Just as in Fig. 13.10, the distance marks can be used for prediction of the azimuthal orientation of the far-field OV displacement if the incident beam wavefront is not plane (see the black, green and cyan curves for $R_c = 50$ cm, $R_c = 85$ cm and $R_c = \infty$, respectively).
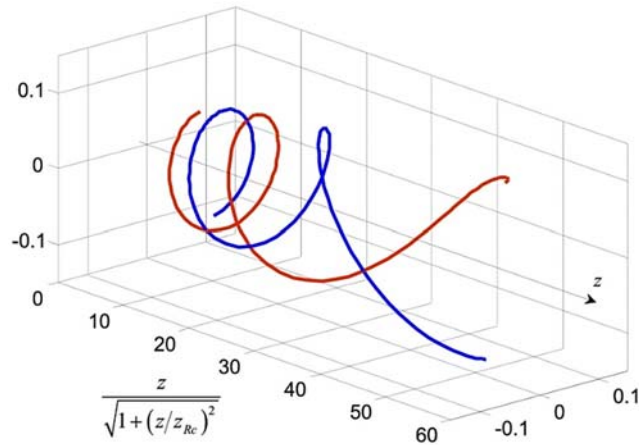
Fig. 13.12. 3D evolution of the OV core positions in the diffracted LG beam (13.9), (13.29) with $m = -2$ and $R_c = \infty$ for $a = 3b_c$. As in Fig. 13.9, the transverse coordinates are in units of b_d (13.31), and the longitudinal coordinate is normalized by the scale factor of (13.31).
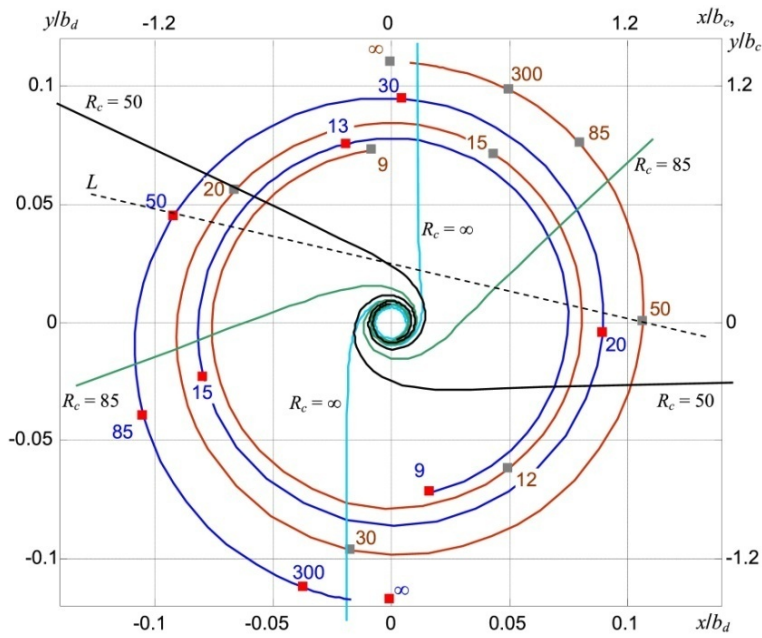
Fig. 13.13. Blue and brown curves represent trajectories of the two secondary OVs formed in the cross section of the diffracted LG beam with $m = -2$ and $a = 3b_c$ (cf. Fig. 13.12), red (grey) rectangles denote the propagation distance (longitudinal coordinate) marked in centimeters, left and bottom scales show the transverse OV coordinates in normalized units (13.31). Black, green and cyan curves are the transverse projections of the secondary-OV trajectories in the modified spherical-front diffracted beams (13.33) (radius of curvature is indicated near each curve, the OV coordinates are measured in units of b_c, and marked in the right and top scales). Dashed line L shows the far-field orientation of the OV pair at $R_c = 50$ cm.

369

Note that the two secondary OVs are always situated opposite with respect to the nominal beam axis *z*. However, they never form a perfect central-symmetric pair (with the centre at the transverse coordinate origin) dictated by the approximate model (13.27) with $M = 0$, except in the asymptotic case $z = \infty$, $R_c = \infty$; this is also a consequence of the slight symmetry perturbation upon the WDP. At the same time, the two secondary OVs define a straight line whose far-field orientation can be distinctly associated with the wavefront curvature of the incident LG beam (see, for example, the dashed line *L* in Fig. 13.13 that unites the two OV cores in case $R_c = 50$ cm). The rotation of this line with the incident wavefront curvature variation is illustrated by the green curve in Fig. 13.11. As in case of $|m| = 1$, its behaviour can be fairly approximated by Eq. (13.37), cf. the green dashed curve in Fig. 13.11. Its main difference from the simulation results is that it does not show the rotation accelerations near $\phi_r = \pi/2$, $3\pi/2$ where one of the OVs crosses the negative *y* half-axis. These accelerations correspond to the trajectories' 'jumps' observed in the diffracted Kummer OV beams (Fig. 13.6 (a)) and can be explained with allowance for the cosine term in (13.27) (see Section 13.7).

In summary, the far-field pattern of the diffracted OV beam supplies an interesting example where the input wavefront curvature is transformed into the output azimuthal rotation of the secondary OV pair, which can possibly find applications for wavefront diagnostics and measurements.

13.6. Discontinuities of the OV Trajectories and Topological Reactions in the Diffracted OV Beams

The previous sections illustrate and explain the main regularities of the OV trajectories and the singular skeleton evolution in diffracted OV beams. Now we proceed with the study of apparent 'irregularities' which so far were beyond our attention. In essence, we will concentrate on the non-uniform velocity of the OV motion along its trajectory (while the screen edge moves uniformly), which is most articulately expressed by the enigmatic 'jump' of the *a*-dependent OV trajectory in Fig. 13.6 (a). In this section based mainly on the recent results of Ref. [33] we are going to elucidate the nature and conditions of this and similar effects.

13.6.1. The 'Jump' Description: Kummer Beams

To this end, we reconsider the *a*-dependent OV trajectories for the diffracted Kummer beam (13.6)–(13.8) with $m = -3$ and parameters

$$k = 10^5 \text{ cm}^{-1}, \ b = 0.232 \text{ mm}, \ R = 54 \text{ cm}, \ z_h = 11 \text{ cm}, \quad (13.38)$$

observed in the cross section $z = 30$ cm behind the screen (see Fig. 13.1 (c)). The results are given in Fig. 13.14 representing a supplemented and re-arranged left column of Fig. 13.6. Panel (a) illustrates the phase distribution in the observed bean cross section; the lines of different colors indicate the constant-phase contours with increment 1 rad (cf. Fig. 13.3 (c)). In Fig. 13.14 (a), three single-charged OVs are seen that originate from

decomposition of the incident 3-charged OV; Figs. 13.14 (b–d) show the trajectories of OVs B–D, respectively.
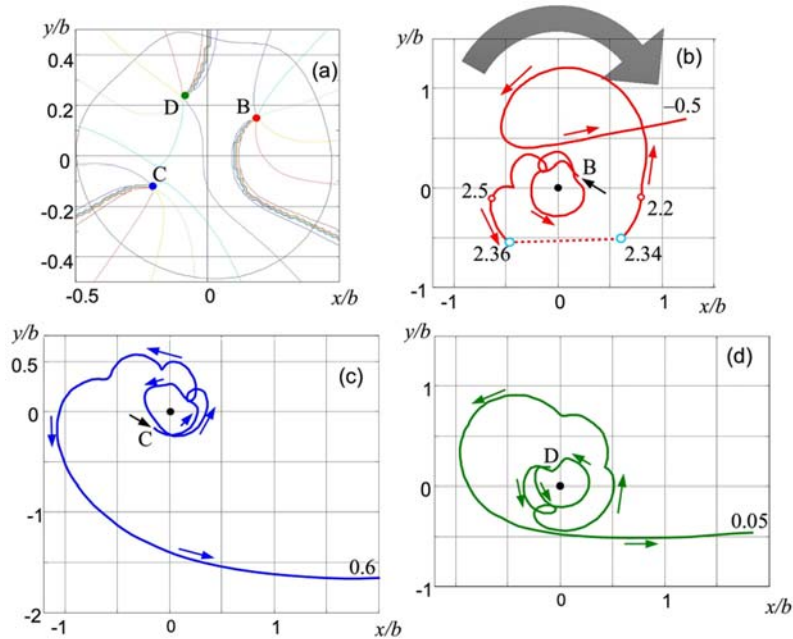
Fig. 13.14. Trajectories described by the OV cores in the cross section $z = 30$ cm behind the screen, the screen edge moving from $a = 4.4b$ to $a = -0.5b$ (see Fig. 13.1 (c)), for the incident Kummer beam with topological charge $m = -3$ and parameters (13.38). The transverse coordinates are expressed in units of b (13.38); large grey arrow shows the energy circulation in the incident beam (cf. Figs. 13.1(a) and 13.3 (b)), small arrows show the directions of the OV motion. (a) 'Initial' positions of the three secondary OVs marked B, C and D for $a = 4.4b$, the thin black curve denotes the constant intensity contour at a level 10 % of the maximum; (b)–(d) trajectories of OVs B, C and D while the screen edge advances (the final values of a / b at which the corresponding OV disappears are marked near the ends of the curves), the beam axis is denoted by the black circle. The dotted line in panel (b) illustrates the OV 'jump'.

The non-uniformity of the OV motion along its trajectory is most impressively evident in the trajectory of the OV B (Fig. 13.14 (b)). While the screen performs a minute advance from $a = 2.36b$ to $a = 2.34b$, the OV abruptly 'jumps' between the points marked by cyan circles so that the trajectory apparently looks discontinuous (compare this with the adjacent trajectory segments where much larger screen shifts from $a = 2.5b$ to $a = 2.36b$ and from $a = 2.34b$ to $a = 2.2b$ cause noticeably smaller changes in the OV positions marked by the red circles). Also, while the OV B performs this 'jump', the positions of other OVs remain practically unchanged. In what follows, we intend to investigate the nature and mechanism of this effect.

To accomplish this, we return to the asymptotic analytical model of Eqs. (13.22), (13.23). We employed these equations in the previous sections but under the assumption that at

the WDP conditions, the off-axial displacements of the OV cores are small enough so that in Eq. (13.16) $M \ll 1$, and the cosine term in the left-hand side of (13.23) can be omitted. However, the trajectory details we are studying in this Section appear at not very small *r*-values when the cosine term cannot be discarded. Subsequently, the equations (13.15) or (13.23) for the azimuthal coordinate of the OV core become transcendent and, in contrast to what was made in Section 13.5, cannot be solved analytically. To inspect the main consequences of the trigonometric term, we investigate the simpler equation (13.15). Its qualitative analysis is illustrated in Fig. 13.15 (a). The left-hand side as a function of ϕ is imaged by the blue curve (for comparison, the thin light-blue line represents the left-hand side in the limiting case $M = 0$), and each horizontal line expresses a certain value of the right-hand side depending on *a* and *z* for a certain secondary OV number *N*. The solution $\phi(a, z)$ is obtained as an intersection of the blue curve and the corresponding horizontal line. In the 'normal' situation, $M = 0$, there is only one intersection point (see, e.g., points ϕ_1 and ϕ_4 in Fig. 13.15 (a)). When applied to the case of $m < 0$ presented in Fig. 13.14, with *a* decreasing monotonically the horizontal line moves upward, and the corresponding $\phi(a, z) = \phi_1$ also changes monotonically and continuously. However, due to the trigonometric term in Eq. (13.15), the left-hand side can be non-monotonic, and at certain values of *a* and *z*, the horizontal line reaches the region where the blue curve is nearly horizontal or decreases (e.g., between the red dashed lines in Fig. 13.15 (a), $\phi_2 < \phi < \phi_3$). Obviously, in this region $\phi(a, z)$ can change very rapidly; besides, there appear additional intersections that testify for nothing but emergence of additional OVs.

The graphical solution of Eqs. (13.22)–(13.16) is performed similarly. Although the evolution of the blue curve is more complicated than was discussed in the above paragraphs because of the variable *M* (13.16), which depends on *a* explicitly as well as implicitly, via *r* and Eq. (13.22), and due to the more complex *a*-dependence of the right-hand side of Eq. (13.23), the principal details remain the same [33].

The existence of several intersections of the horizontal line with the blue curve (as for the green line in Fig. 13.15 (a)) means that the smooth translational migration of the OV is no longer possible and is thus replaced by the topological reaction in which additional OVs emerge and annihilate [4]. Images of Figs. 13.15 (b–d) show the numerical example explaining the behavior of the OV B whose trajectory is depicted in Fig. 13.14 (b), within the 'jump' region. The OV positions are marked by the corresponding letters, as in Fig. 13.14 (b–d); additionally they are provided with curved arrows showing the local direction of transverse energy circulation, colored in agreement with the trajectory colors in Figs. 13.6 and 13.14. While *a* approaches the 'jump' region ($a = 2.36$ in Fig. 13.14 (b), point ϕ_2 in Fig. 13.15 (a)), there are three secondary OVs presented in Fig. 13.15 (b). At this moment, the small screen advancement towards the axis almost does not affect the OV positions but induces a topological event: in the area indicated by the black circle in Fig. 13.15 (b), the cut is torn and the dipole of oppositely charged OVs emerges (see Fig. 13.15 (c)). With further decrease of *a*, one of the new-born OVs, V, charged oppositely to all the other OVs (black curve arrow), rapidly moves against the 'normal' spiral OV motion. Subsequently it meets the OV B and annihilates with it, whereas the second member of the dipole pair, B', still remains and starts its migration as a

'continuation' of the OV B (Fig. 13.15 (d)). Note that singularities C and D are practically stable during this process, and the 'virtual' OV V moves from B' to B along the smooth arc looking as a natural 'filling' of the spiral-like trajectory between $a = 2.36$ and $a = 2.34$. This agrees with the approximate Eq. (13.22) that dictates that radial coordinates of all OVs, including the 'virtual' ones, are determined by a and z independently of the azimuth ϕ.
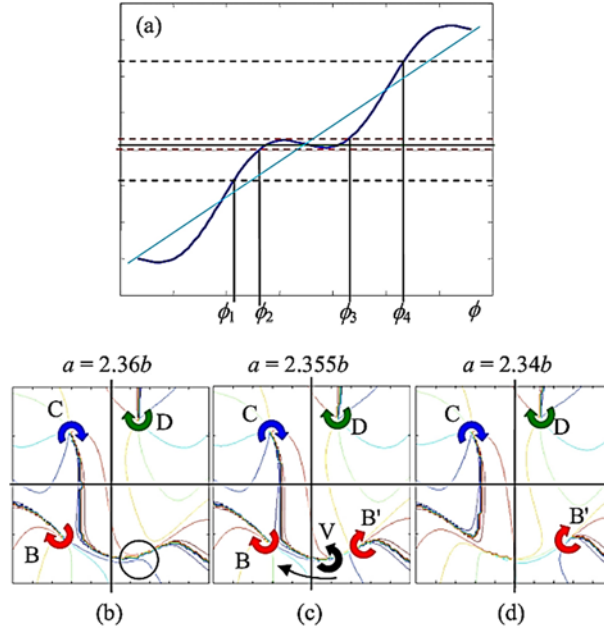
Fig. 13.15. (a) Illustration for the solution of Eqs. (13.15) and (13.23): The blue curve is the plot of the left-hand side expression for $|M| = 1.4$, horizontal lines symbolize different (a, z)-dependent values of the right-hand side. (b)–(d) Equiphase contours and the secondary OV positions in the cross section of the diffracted beam of Fig. 13.14; curve arrows show the local energy circulation near the OV cores; the screen-edge positions are indicated above each panel (further explanations in text).

The described anomalies of the OV trajectories in the diffracted beam are caused by the non-monotonic character of the left-hand side of Eq. (13.15) or (13.23), which takes place if the 'jump criterion' is realized,

$$|M| = \left|\frac{kra}{mz}\right| > 1, \tag{13.39}$$

and near the points where

$$\cos\phi = 0, \quad \frac{d}{d\phi}(M\cos\phi) < 0. \tag{13.40}$$

The latter condition explains why the jump of Fig. 13.14 (b), as well as the noticeable acceleration of the OV motion in Figs. 13.14 (c, d) [21] occur in the lower half-plane, near $\phi = 3\pi/2$ (remember that $m < 0$ and, consequently, $M < 0$); this is also the reason for the 'steep' segments of the solid curves in Fig. 13.7 (d) near the points where $\phi = -\pi/2, 3\pi/2, 7\pi/2$. In turn, Eq. (13.39) shows that the 'jump' can preferably take place at large enough a and not very high z; in particular, this explains why the numerical analysis reveals the 'jump' anomalies at $z = 30$ cm but they cannot be detected, with the same incident beam, at $z = 60$ cm and $z = 82$ cm (see Fig. 13.6). In the present conditions of Eq. (13.38) and Fig. 13.14 (b) with $z = 30$ cm, $a = 2.35b$, $r \approx 0.72b$, one finds $|M| \approx 1.01$, which agrees with the 'jump' existence. Noteworthy, the trajectories of the OVs C and D differ from the considered OV-B trajectory by the values of a and r at which they traverse the vicinity of $\phi = 3\pi/2$. For the OV C this occurs at $a = 3.75b$, $r \approx 0.25b$ (Fig. 13.14 (c)), which gives $|M| = 0.56$; for the OV D – at $a = 3.1b$, $r \approx 0.4b$ (Fig. 13.14 (d)) whence $|M| = 0.74$. This completely agrees with the absence of jumps and accompanying topological events in trajectories C and D. Similarly, one can easily verify that $|M| < 1$ for all curves of Figs. 13.4–13.6, except Fig. 13.6 (a) and the red curve in Fig. 13.6 (j).

### 13.6.2. Discontinuities in the Laguerre-Gaussian Beams' Diffraction

Now let us consider the singular skeleton evolution upon diffraction of the LG beam (13.9). Instead of the previously analyzed beam with parameters (13.11), here we choose another example that enables us to expose the special features of the OV trajectories more explicitly: we take the LG beam with $m = -3$ and assume in the calculations the following values for the beam parameters:

$$k = 10^5 \text{ cm}^{-1}, \quad b_c = b_0 = b = 0.232 \text{ mm}, \quad z_c = 0, \quad R_c = \infty, \qquad (13.41)$$

(like in Section 13.5.1, the beam waist coincides with the screen plane). The numerically calculated OV trajectories in the diffracted beam cross section are presented in Fig. 13.16. As in the Kummer beam case (Fig. 13.14), there are three secondary OVs that evolve along the spiral-like trajectories and consecutively move to the shadow region where they vanish. The trajectories are marked by the same colors and the same letter notations as their counterparts in Fig. 13.14 (b–d). As expected, they show more regular and smooth behavior than in the case of a Kummer beam, which is associated with the slower decay and oscillations of the Kummer beam intensity at $r >> b$ [21, 34] (see the remarks in the penultimate paragraph of Section 13.4.2). Accordingly, the analytical model of Section 13.4.2 not only provides qualitative but also a fair quantitative characterization of the trajectory B even if $a \approx b$, cf. Fig. 13.16(a) where the trajectory obtained analytically from Eqs. (13.26), (13.27) with $M = 0$ is presented as the thin dotted spiral; note that its final point corresponds to $a = 1.2b$.

Upon calculations, the 'jumps' were identified as events for which an additional pair of OVs emerge. For example, in Fig. 13.16 (a), while a decreases, the 'red' OV with topological charge –1 moves along the segment B_0B and at the moment it approaches point B, the OV dipole is distinguished with –1-charged OV in point B'. This event takes place at $a = 1.98b$; then, the oppositely charged dipole member – 'virtual' OV V – rapidly

moves along the black arc against the main spiral evolution. Meanwhile, the 'old' OV still continues its slow motion to meet the 'virtual' one until the annihilation occurs in the point marked by the circle at $a = 1.94b$.[1] During the entire process, the OV radial coordinate remains approximately constant, $r = 0.44b$. Similar events happen to the OV C at $a = 2.92b$ to $2.90b$ (Fig. 13.16 (b), $r = 0.27b$) and to the OV D at $a = 2.52b$ to $2.48b$ (Fig. 13.16 (c), $r = 0.35b$). In contrast to the situation of Fig. 13.14, now all the OVs experience rather articulate 'jumps', which is explained by the high values of the jump factor (13.39): $|M| = 1.56$, 1.40 and 1.57 in cases of Fig. 13.16 (a–c), correspondingly.
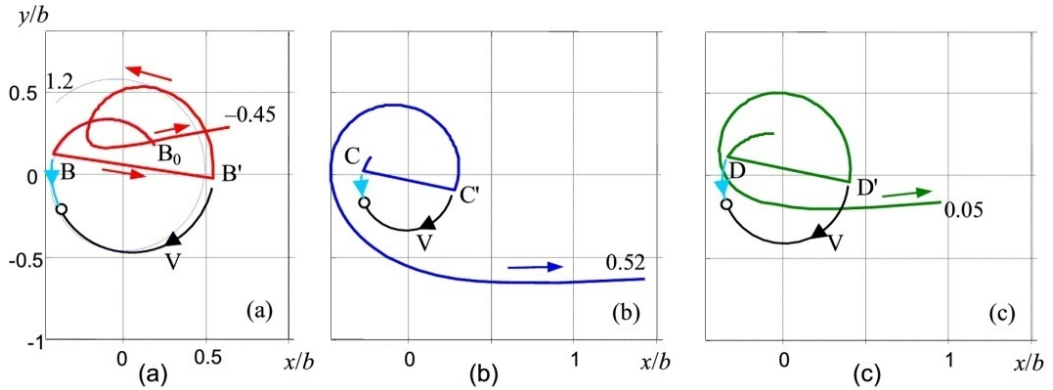
Fig. 13.16. Trajectories described by the OV cores in the cross section $z = 10$ cm behind the screen, the screen edge moving from $a = 3b$ to $a = -0.45b$ (see Fig. 13.1 (a)), for the incident LG beam with topological charge $m = -3$ and parameters (13.41). Each panel shows the trajectory of a single OV with additional explanatory details. The transverse coordinates are expressed in units of b (13.41), small arrows show the directions of the OV motion; the final values of a / b at which the corresponding OV disappears are marked near the ends of the curves. The trajectories experience 'jumps' between points B and B', C and C', D and D', respectively; the black (cyan) arcs represent the motion of 'virtual' ('old') OVs before their annihilation in points marked by circles. In panel (a), the trajectory calculated analytically via Eqs. (13.26), (13.27) for $3b > a > 1.2b$ with $M = 0$ is depicted by the thin dotted curve for comparison.

13.7. OV Jumps in the z-Dependent Singular Skeleton Evolution

According to the general physical arguments based on the analytical suggestions supplied by Eqs. (13.14), (13.15), (13.22), (13.23), (13.26) and (13.27), the discussed mechanisms determining the OV trajectories are still in charge of the z-dependent evolution, and the trajectory discontinuities and topological reactions of the above-described type are expected to occur in this situation as they do in the a-dependent trajectories studied in Section 13.6. Some examples below will illustrate the relevant processes.

---

[1]Note that the 'virtual' OV distantly resembles the virtual particles in quantum theory [37]: it is short-lived, and its only role is to implement the reaction transforming B into B'

13.7.1. Kummer Beams

Fig. 13.17 represents the *z*-dependent evolution of the secondary OVs in the same diffracted beam that was analyzed in Section 13.3.3, Fig. 13.6 (left column) and Section 13.6.1, Fig. 13.14 but for the fixed screen-edge position $a = 4b$ illustrated in the panel (a). Note that, to make the beam structure better visible, the transverse amplitude distribution $\left| u^K \left(x_a, y_a, z_h \right) \right|$ is presented instead of the more common intensity $\left| u^K \left(x_a, y_a, z_h \right) \right|^2$. Anyway, the screen barely 'touches' the beam periphery, which, nevertheless, induces rich of details and quite observable perturbations of its singular skeleton displayed in Fig. 13.17 (b–d). In case of a propagating beam, there always is present the trivial component of the OV migration associated with the overall beam divergence; to abstract from this non-informative component, in Fig. 13.17 (b–d) the OV trajectories are displayed in the normalized transverse coordinates

$$x_e = x \left(1 + \frac{z}{R} \right)^{-1}, \quad y_e = y \left(1 + \frac{z}{R} \right)^{-1}. \tag{13.42}$$

In general, the OV trajectories of Fig. 13.17 (b–d) are similar to those of Fig. 13.14 (b–d) and show the same character of pulsating spirals. In the course of diffracted beam propagation (growing *z*), the pulsation period increases and in the far field the pulsations vanish. In contrast to the trajectories of Figs. 13.6 and 13.14, here are no self-crossings ('loops' as in Figs. 13.14 (b–d)); the apparent self-crossings near $z = 20$ cm in Fig. 13.17 (d) are illusive and appear only in the normalized coordinates (13.42). The most important feature is that in case of the *z*-dependent evolution there also exist regions of very rapid OV migration (the trajectories' segments between the white-filled circles). In full agreement with the model of Section 13.6.1 (see Eq. (13.40) and Fig. 13.15 (a)), these regions are in the lower half-plane (near the OV core azimuth $\phi = 3\pi/2$). However, the 'true' jump only happens to the OV D in the panel (d). This agrees with the criterion (13.39) that can be checked based on the presented trajectories: in Fig. 13.17 (b), $r = 0.18b$, $z = 14$ cm, and $|M| = 0.97$; in Fig. 13.17 (c), $r = 0.226b$, $z = 17.4$ cm, and $|M| = 0.93$; and only in Fig. 13.17 (d) $r = 0.171b$, $z = 11.4$ cm, $|M| = 1.08$ – the conditions for the jump are realized, and it is indeed observed.

13.7.2. Laguerre-Gaussian Beams

Diffraction of an LG beam provides additional and rather conspicuous illustrations for the 3D singular skeleton evolution [23, 33]. Like in Section 13.6.2, we consider the incident LG beam (13.9) with its waist in the screen plane and the Gaussian envelope parameters (13.41) but with the topological charge $m = -2$ (Fig. 13.18).

Despite that the chosen screen edge position $a = 2b$ can hardly be treated as a far periphery of the incident beam profile and the expected perturbation of its structure is rather strong, the OV migration looks remarkably regular (Fig. 13.18 (b)). As in Section 13.5, to remove the trivial migration component associated with the beam divergence, the coordinates are

normalized by the Gaussian envelope radius (13.31) of the supposed unperturbed incident beam, where, in view of Eq. (13.41), $z_{Rc} = z_R = 53.8$ cm is the Rayleigh length of the incident beam. Again, as was noted during comparison of Figs. 13.16 and 13.14, the OV trajectories in the diffracted LG beam form almost perfect spirals, without pulsating irregularities observed in Figs. 13.17 (b–d) for the diffracted Kummer beam.
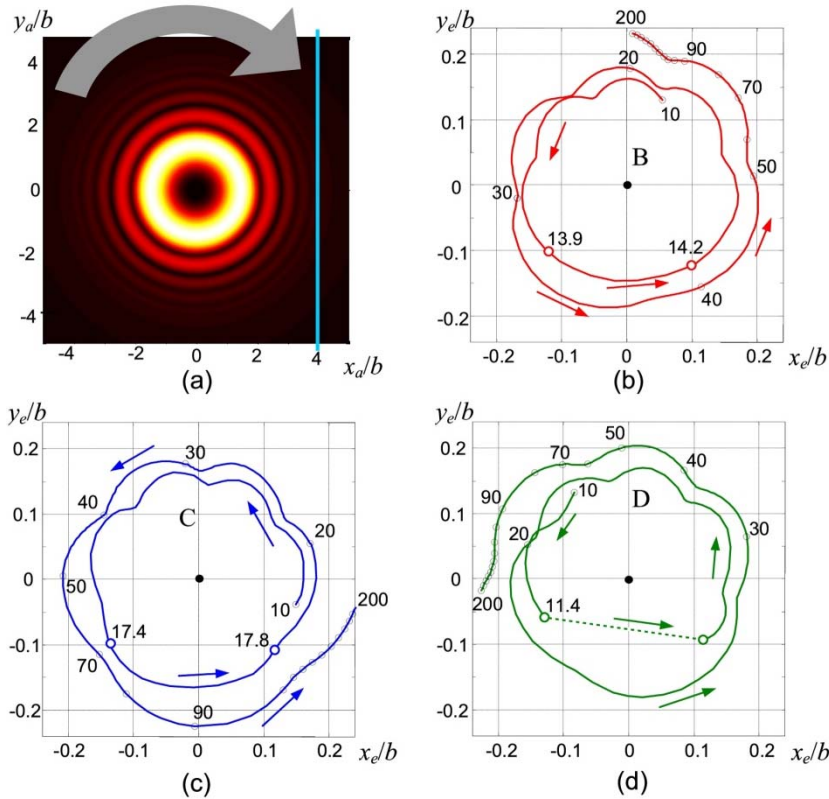
Fig. 13.17. Transverse projections of the OV trajectories behind the screen whose edge is fixed at $a = 4b$ (see Fig. 13.1(a)), for the incident Kummer beam with topological charge $m = -3$ and parameters (13.38) (cf. Fig. 13.14). (a) The screen edge position (blue line) against the incident beam amplitude distribution in the screen plane, the large arrow shows the energy circulation direction. (b)–(d) Separate OV trajectories for z growing from 10 cm to 200 cm, letters B, C and D denote the same secondary OVs that are shown in left column of Fig. 13.6 and in Fig. 13.14; thin black empty circles correspond to z values multiple of ten in centimeters, some of them are provided with corresponding numerical marks; colored white-filled circles mark the segments of rapid evolution. The horizontal and vertical coordinates are in normalized units of (13.42); small arrows show the directions of the OV motion. The trajectory 'jump' is seen only in panel (d) at $z = 11.4$ cm (dotted line).

In Fig. 13.18 (b) the OV B trajectory (red) experiences the jump at $z = 7.05$ cm while the OV C (blue) only shows the rapid evolution between $z = 13.1$ cm and $z = 13.7$ cm. This, again, is in full compliance with the criteria (13.39) and (13.40): for the OV C, $r = 0.234b$,

and with $m = -2$, $a = 2b$, $z = 13.1$ cm this entails $|M| = 0.96$ whereas for the OV B, $r = 0.191b$, $z = 7.05$ cm, and $|M| = 1.46$. The jump mechanism is completely the same as in other examples: the OV dipole is born in point B' after which its oppositely charged 'virtual' member V rapidly moves 'backward' towards the 'old' B and annihilates with it in point A corresponding to $z = 7.65$ cm. This example supplies a spectacular dynamical illustration of the topological reactions and the 'virtual' OV migration accompanying the jump.
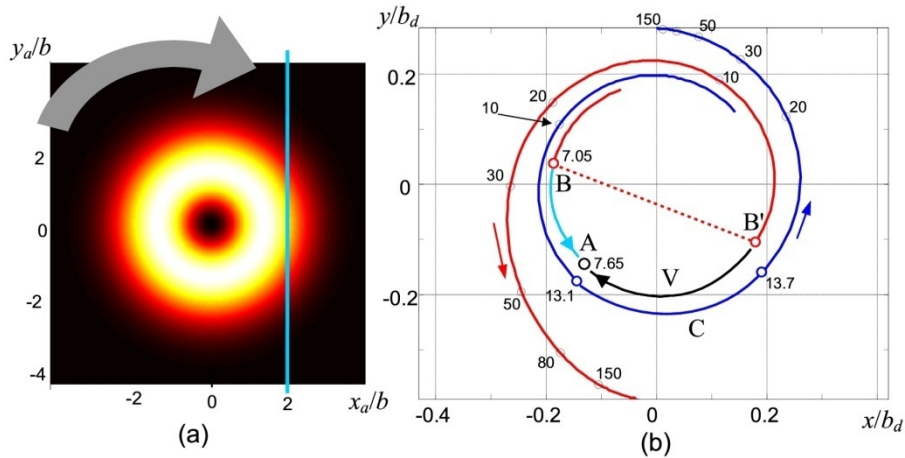
Fig. 13.18. Transverse projections of the OV trajectories behind the screen whose edge is fixed at $a = 2b$ (see Fig. 13.1 (a)), for the incident LG beam with topological charge $m = -2$ and parameters (13.41). (a) The screen edge position (blue line) against the incident beam amplitude distribution in the screen plane, the large arrow shows the energy circulation direction. (b) Red (B) and blue (C) curves represent the trajectories of the two secondary OVs for z growing from 5.6 cm to 530 cm ($9.85z_{Rc}$); black empty circles denote the intermediate z values (marked in centimeters); colored white-filled circles mark the segments of rapid evolution The transverse coordinates are given in units normalized by (13.31); small arrows show the directions of the OV motion. At $z = 7.05$ cm, the OV B experiences the 'jump' into B' position shown by the dotted line; the cyan and black arcs represent the evolution of the 'old' OV B and of the 'virtual' OV V after the jump until they annihilate in the point A marked by the black empty circle.

13.7.3. 3D Trajectories and the Nature of Discontinuities

To elucidate in more detail the discontinuous trajectory of the OV B in Fig. 13.18 (b), we present it as a 3D graph together with the trajectories of the 'old' OV B after the jump and of the virtual OV (cyan and black curves of Fig. 13.18 (b)). The result given in Fig. 13.19 reveals that the three trajectories of Fig. 13.18 (b) are actually fragments of the single 'full' curve that is perfectly continuous and smooth, so the jumps and topological reactions appear only in its projections (in particular, the red, cyan and black curves of Fig. 13.18 (b) are projections of the corresponding segments of the curve of Fig. 13.19 viewed from the positive end of axis z). This agrees with the usual concepts of the OV filaments [6, 38, 39] and discloses the nature of the intriguing effects considered in the previous sections.
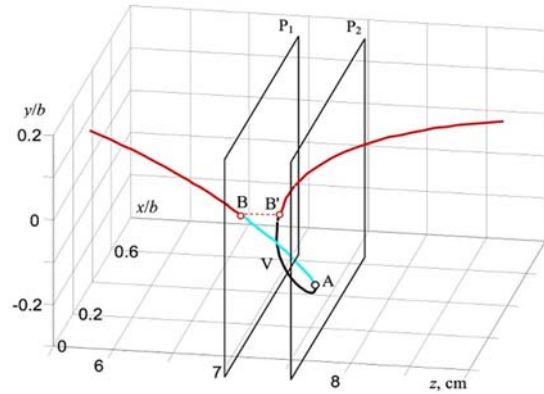
Fig. 13.19. 3D trajectory of the 'red' (B) OV of Fig. 13.18 (b) (incident LG beam with $m = -2$ and parameters (13.41), screen edge position $a = 2b$) in the near-jump region (5.6 cm $< z <$ 9 cm). The transverse coordinates are given in units of b (13.41); plane P_1 ($z = 7.05$ cm) crosses the trajectory in point B and is tangent to it in point B', plane P_2 ($z = 7.65$ cm) is tangent to the trajectory in the annihilation point A (black empty circle); the red, cyan and black segments correspond to the red, cyan and black arcs in Fig. 13.18 (b).

Let the 'full' OV trajectory of Fig. 13.19 be represented in parametrical form, i.e. the coordinates of a current trajectory point are expressed as functions of the trajectory length s measured from the starting point, say, at $z = 5.6$ cm:

$$x_v = x_v(s), \quad y_v = y_v(s), \quad z_v = z_v(s). \qquad (13.43)$$

In a given transverse plane, the OV position is determined as an intersection between the plane and the trajectory. The 'normal' evolution implies that $dz_v/ds > 0$ everywhere, and then in each observation plane only one intersection point can exist; however, in some configurations of the diffracted beam singular skeleton, regions of a 'retrograde' evolution, where

$$dz_v/ds < 0, \qquad (13.44)$$

may occur. It is such a situation that is depicted in Fig. 13.19 between the transverse planes P_1 and P_2. When the observation plane approaches P_1 from the left, it 'touches' the trajectory at the additional point B' (a local minimum of the function $z_v(s)$), which corresponds to the dipole emergence. With further advance, the observation plane will contain three intersection points with the curve, which are interpreted as the 'teleported' OV B', 'old' OV B and the 'virtual' oppositely charged OV V. In the position P_2 the observation plane again touches the trajectory, now in point A with the local maximum of $z_v(s)$, and the intersections corresponding to B and V disappear: the two OVs annihilate.

This picture completely explains the discontinuous trajectories of the OV cores not only in case of the z-dependent evolution (Sections 13.7.1, 13.7.2) but also in case of the screen edge translation (Section 13.6). In the latter situation, the observation plane is fixed but

379

the 'full' 3D curve is smoothly deformed with variation of a, and the 2D trajectory jump takes place if in the observation plane the condition (13.44) becomes true. In fact, the 'jump criterion' (13.39) is equivalent to (13.44), and this is why it is equally applicable to both the z-dependent and a-dependent variations of the diffracted beam singular skeleton.

Here we are touching the aspect in which the theory of OV diffraction becomes entangled into the rich and stimulating field of the vortex lines and their geometry (see, e.g., [6] and references therein). This aspect deserves a special investigation; now we only remark that the intricate and at first glance artificial patterns of the OV lines that are deliberately generated by means of special procedures [6, 39] can naturally exist in the edge-diffracted circular OV beams.

13.8. Conclusion

The main results presented in this chapter testify that the simple and ubiquitous situation of edge diffraction provides additional impressive manifestations of the helical nature of light beams with OV. The diffraction obstacle introduces the beam perturbation that causes the OV displacement from its original axial position (for an m-charged OV, $|m|$ single-charged displaced OVs are formed around the axis). Then, while the diffracted beam freely propagates (z-dependent evolution), the displaced OVs migrate over the beam cross section along spiral-like trajectories, initially (at small post-screen distances) with high rotation rate, which rapidly decreases and practically stops far enough behind the screen. The similar OV migration takes place in a fixed cross section when the screen edge moves towards the beam axis (a-dependent evolution), in compliance with the approximate relations (13.32) or (13.15). The most articulate spiral-like trajectories occur under conditions of weak diffraction perturbation (WDP), when the screen edge is separated from the incident beam axis by two or more beam radii, i.e. when the beam circular shape is almost unaffected by the diffraction. This puts certain limitations to the practical employment of the predicted behavior, since the off-axial OV displacements are small and their measurement may impose difficulties. However, we emphasize the principal importance of the predicted features and their close relation with the physical nature of OVs. Besides, at least for a multicharged OV diffraction, even under the WDP conditions, the typical OV displacement can reach ~10 % of the current beam radius b (see Figs. 13.5, 13.6, 13.12, 13.13–13.18), which is quite measurable.

It should be noted that the observed and predicted peculiar details of the singular skeleton behavior are rather common for light beams with well-developed singular structure, e.g. speckle fields [4, 6]. In this view, the diffracted OV beams can be considered as their simplified models and, possibly, produce efficient means to create controllable singular-optics structures with prescribed properties, which can be useful in diverse research and technology applications.

In particular, the presence of the well-developed, regular and easily interpretable singular structure makes the diffracted OV beams suitable objects for the general study of the OV filaments and their geometric regulations, evolution of individual singularities, their transformations, topological reactions and interactions. On the other hand, the OV

trajectories' discontinuities, 'jumps', birth and annihilation events described in this Chapter are, as a rule, highly sensitive to the incident beam parameters and the diffraction conditions. For example, the OV positions in the diffracted beam cross section can be sensitive indicators of the screen edge position with respect to the incident beam axis, which can be employed for precise distant measurements of small displacements and deformations [15, 19]. From Figs. 13.16 (b) and 13.18 one can easily see that near the 'threshold' conditions of topological reactions, the screen edge displacement of $0.01b$ induces a two orders of magnitude larger OV jump in the diffracted beam cross section. Note that such sensitivity is predicted without any special consideration; undoubtedly, a detailed analysis aimed at the search of the diffraction parameters most favorable for the distant metrology will improve these figures. This aspect of the present work enables us to suggest its applications for the problems of the precise OV metrology [29–32] as well as for the incident OV diagnostics, which can be prospective in the fields of laser beam shaping and analysis and in optical probing systems.

Additional interesting possibilities are associated with relations between the incident beam wavefront curvature and the diffracted beam structure. First, we have refined the earlier statements [15, 19] that in the far field, the diffracted circular OV beam acquires the symmetry with respect to an axis parallel to the screen edge. In fact, this symmetry is only realized in the beam's Fraunhofer (Fourier) plane, which can be real (if the beam converges, radius of curvature $R_c < 0$) or imaginary (if $R_c > 0$), and only for beams with plane wavefront it occurs at the propagation infinity (in the extreme far field). Importantly, the actual far-field pattern of the diffracted beam essentially depends on the incident beam wavefront curvature. In terms of the OV displacements, any change of the incident beam wavefront curvature–while preserving the intensity profile–induces the azimuthal rotation of the far-field OV position in the diffracted beam. This sensitivity may be useful for the OV beam diagnostic and for the wavefront measurements.

Most of the quantitative results of this Chapter are obtained numerically but their interpretation is based on the asymptotic analytical model of Eqs. (13.15)–(13.17) with refinements (13.22), (13.23) and (13.26), (13.27). Remarkably, the model derived for the condition $a \gg b$ appears to be valid in the much larger and physically interesting domain; at least, for the LG beam diffraction it does not fail even at $a \approx 2b$, and the model-based criterion (13.39) works perfectly well in all the considered examples. However, the model predicts monotonic behavior of the OV radial displacement r with growing z for Kummer beams, i.e. does not explain the radial pulsations of the spirals in Fig. 13.17 (b–d). Nevertheless, we hope that despite its approximate character, the model will give a reliable analytical basis for further research of the vortex beams' diffraction. At least, all the conclusions concerning the spiral-like character of the OV trajectories and their jumps when the criteria (13.39) and (13.40) are satisfied, are absolutely reliable and supported by experiment [20, 21]. The fine details of the OV trajectories in diffracted Kummer beams (self-crossings and pulsations in Figs. 13.14 (b–d) and 13.17 (b–d)), that appear due to the slow fall-off of the Kummer beam amplitude, are expected to be sensitive to the incident beam behavior at the far transverse periphery. In this view, even the 'routine' approximations usually employed in the numerical simulations can become sources of errors, e.g., the integration domain limitation in the Fresnel–Kirchhoff integral (13.4). In

such situations, the explicit allowance for the specific conditions of the Kummer beam preparation and for the optical system it passes would be necessary.

A possible direction for further research can be related with a more comprehensive characterization of the separate OVs in the diffracted beam. So far we were only interested in their positions; but no less informative can be their morphology and anisotropy parameters [5, 6]: the orientation and the axes ratio of the equal-intensity ellipses in the nearest vicinity of the OV core. Especially, under conditions close to topological reactions, the OVs are highly anisotropic, and this supplies additional markers to characterize the qualitative discontinuities in the singular skeleton evolution. Another way of possible further development of ideas and approaches introduced in the present work can be oriented at the search of special conditions of the OV beam preparation and diffraction, which provide high sensitivity for the metrological and diagnostic applications outlined two paragraphs above.

Finally, we would like to note that the edge diffraction can be considered a special case of the OV beam transformation with symmetry violation. The specific response of OV beams to their symmetry breakdown is interesting from a fundamental point of view and supplies efficient means for their investigation and diagnostics [5, 14, 16, 18, 40, 41]. There is a wide variety of such transformations; in particular, the astigmatic focusing and telescopic transformations of OVs are studied in much detail (see, e.g., [42–44]). But they show quite different behavior of the secondary OVs within the transformed beam cross section, most likely due to preserving the central symmetry of the beam transverse profile. However, one can expect that some features of the OV migration, similar to those considered in this chapter, can be detected in OV beams subjected to the symmetry violation which destroys the central symmetry. It would be meaningful and instructive to inspect the response of an OV beam to the unilateral beam constraint, e.g., by a "soft" diaphragm, or even unilateral phase modification in some peripheral part of the beam cross section. These transformations are, properly, special cases of diffraction but they admit more 'gentle' conditions suppressing the edge waves, diffraction fringes [2], etc., which will be favourable for precise measurements.

Acknowledgements

References

[1]. M. Born, E. Wolf, Principles of Optics, *Cambridge University Press*, 1999.
[2]. S. Solimeno, B. Crosignani, P. DiPorto, Guiding, Diffraction and Confinement of Optical Radiation, *Academic Press*, 1986.

[3]. H. Rubinsztein-Dunlop, A. Forbes, M. V. Berry, M. R. Dennis, D. L. Andrews, M. Mansuripur, C. Denz, C. Alpmann, P. Banzer, et al., Roadmap on structured light, *J. Opt.*, Vol. 19, Issue 1, 2017, 013001.

[4]. M. S. Soskin, M. V. Vasnetsov, Singular optics, *Prog. Opt.*, Vol. 42, 2001, pp. 219–276.

[5]. A. Ya. Bekshaev, M. S. Soskin, M. V. Vasnetsov, Paraxial Light Beams with Angular Momentum, *Nova Science Publishers*, 2008.

[6]. M. R. Dennis, K. O'Holleran, M. J. Padgett, Singular optics: optical vortices and polarization singularities, *Prog. Opt.*, Vol. 53, 2009, pp. 293–364.

[7]. I. G. Marienko, M. V. Vasnetsov, M. S. Soskin, Diffraction of optical vortices, *Proceedings of SPIE*, Vol. 3904, 1999, pp. 27–34.

[8]. M. V. Vasnetsov, I. G. Marienko, M. S. Soskin, Self-reconstruction of an optical vortex, *JETP Lett.*, Vol. 71, Issue 4, 2000, pp. 130–133.

[9]. J. Arlt, Handedness and azimuthal energy flow of optical vortex beams, *J. Mod. Opt.*, Vol. 50, Issue 10, 2003, pp. 1573–1580.

[10]. V. N. Gorshkov, A. N. Kononenko, M. S. Soskin, Diffraction and self-restoration of a severe screened vortex beam, *Proceedings of SPIE*, Vol. 4403, 2001, pp. 127–137.

[11]. J. Masajada. Gaussian beams with optical vortex of charge 2- and 3-diffraction by a half-plane and slit, *Optica Applicata*, Vol. 30, Issue 2–3, 2000, pp. 248–256.

[12].J. Masajada, Half-plane diffraction in the case of Gaussian beams containing an optical vortex, *Opt. Commun.*, Vol. 175, Issue 4–6, 2000, pp. 289–294.

[13]. H. X. Cui, X. L. Wang, B. Gu, Y. N. Li, J. Chen, H. T. Wang, Angular diffraction of an optical vortex induced by the Gouy phase, *J. Opt.*, Vol. 14, Issue 5, 2012, 055707.

[14]. A. Ya. Bekshaev, K. A. Mohammed, I. A. Kurka, Transverse energy circulation and the edge diffraction of an optical-vortex beam, *Appl. Opt.*, Vol. 53, Issue 10, 2014, pp. B27–B37.

[15]. A. Bekshaev, K. A. Mohammed, Transverse energy redistribution upon edge diffraction of a paraxial laser beam with optical vortex, *Proceedings of SPIE*, Vol. 9066, 2013, 906602.

[16]. A. Bekshaev, K. Bliokh, M. Soskin, Internal flows and energy circulation in light beams, *J. Opt.*, Vol. 13, Issue 5, 2011, 053001.

[17]. K. Volke-Sepulveda, R. A. Terborg, Can diffraction provide quantitative information about energy flux in an optical vortex?, in *Proceedings of the Frontiers in Optics/Laser Science Conference* (*FIO/LS'11*), *OSA Technical Digest*, San Jose, CA, United States, 16–20 Oct. 2011, pp. JTuA38.

[18]. A. Y. Bekshaev, I. A. Kurka, K. A. Mohammed, I. I. Slobodeniuk, Wide-slit diffraction and wavefront diagnostics of optical-vortex beams, *Ukr. J. Phys. Opt.*, Vol. 16, Issue 1, 2015, pp. 17-23.

[19]. A. Ya. Bekshaev, K. A. Mohammed, Spatial profile and singularities of the edge-diffracted beam with a multicharged optical vortex, *Opt. Commun.*, Vol. 341, 2015, pp. 284–294.

[20]. A. Chernykh, A. Bekshaev, A. Khoroshun, L. Mikhaylovskaya, A. Akhmerov, K. A. Mohammed, Edge diffraction of optical-vortex beams formed by means of the "fork" hologram, *Proceedings of SPIE*, Vol. 9809, 2015, 980902.

[21]. A. Bekshaev, A. Chernykh, A. Khoroshun, L. Mikhaylovskaya, Localization and migration of phase singularities in the edge-diffracted optical-vortex beams, *J. Opt.*, Vol. 18, Issue 2, 2016, 024011.

[22]. A. Bekshaev, L. Mikhaylovskaya, A. Chernykh, A. Khoroshun, Evolution of the phase singularities in edge-diffracted optical-vortex beams, **in *Proceedings of the IEEE 7th International Conference on Advanced Optoelectronics and Lasers (CAOL'16),* Odessa, Ukraine, 12–15 Sept. 2016, pp. 23–25.

[23]. A. Bekshaev, A. Chernykh, A. Khoroshun, L. Mikhaylovskaya, Displacements and evolution of optical vortices in edge-diffracted Laguerre-Gaussian beams, *J. Opt.*, Vol. 19, Issue 5, 2017, 055605.

[24]. M. Chen, F. S. Roux, J. C. Olivier, Detection of phase singularities with a Shack–Hartmann wavefront sensor, *J. Opt. Soc. Am. A*, Vol. 24, Issue 7, 2007, pp. 1994–2002.

[25]. K. Murphy, D. Burke, N. Devaney, C. Dainty, Experimental detection of optical vortices with a Shack-Hartmann wavefront sensor, *Opt. Express*, Vol. 18, Issue 15, 2010, pp. 15448–15450.

[26]. O. V. Angelsky, S. G. Hanson, A. P. Maksimyak, P. P. Maksimyak, On the feasibility for determining the amplitude zeroes in polychromatic fields, *Opt. Express*, Vol. 13, Issue 12, 2005, pp. 4396-4405.

[27]. W. Wang, T. Yokozeki, R. Ishijima, A. Wada, Y. Miyamoto, M. Takeda, S. G. Hanson, Optical vortex metrology for nanometric speckle displacement measurement, *Opt. Express*, Vol. 14, Issue 1, 2006, pp. 120–127.

[28]. A. M. S. Maallo, P. F. Almoro, Numerical correction of optical vortex using a wrapped phase map analysis algorithm, *Opt. Lett.*, Vol. 36, Issue 7, 2011, pp. 1251–1253.

[29]. M. R. Dennis, J. B. Götte, Topological aberration of optical vortex beams: Determining dielectric interfaces by optical singularity shifts, *Phys. Rev. Lett.*, Vol. 109, Issue 18, 2012, 183903.

[30]. A. Popiołek-Masajada, B. Sokolenko, I. Augustyniak, J. Masajada, A. Khoroshun, M. Bacia, Optical vortex scanning in an aperture limited system, *Optics and Lasers in Engineering*, Vol. 55, 2014, pp. 105–112.

[31]. D. Wojnowski, E. Jankowska, J. Masajada, J. Suszek, I. Augustyniak, A. Popiolek-Masajada, I. Ducin, K. Kakarenko, M. Sypek, Surface profilometry with binary axicon-vortex and lens-vortex optical elements, *Opt. Lett.*, Vol. 39, Issue 1, 2014, pp. 119–122.

[32]. Ł. Płocinniczak, A. Popiołek-Masajada, J. Masajada, M. Szatkowski, Analytical model of the optical vortex microscope, *Appl. Opt.*, Vol. 55, Issue 12, 2016, pp. B20–B27.

[33]. A. Bekshaev, A. Chernykh, A. Khoroshun, L. Mikhaylovskaya, Singular skeleton evolution and topological reactions in edge-diffracted circular optical-vortex beams, *Opt. Commun.*, Vol. 397, 2017, pp. 72–83.

[34]. A. Ya. Bekshaev, A. I. Karamoch, Spatial characteristics of vortex light beams produced by diffraction gratings with embedded phase singularity, *Opt. Commun.*, Vol. 281, Issue 6, 2008, pp. 1366–1374.

[35]. A. Bekshaev, O. Orlinska, M. Vasnetsov, Optical vortex generation with a "fork" hologram under conditions of high-angle diffraction, *Opt. Commun.*, Vol. 283, Issue 10, 2010, pp. 2006–2016.

[36]. M. Abramovitz, I. Stegun, Handbook of Mathematical Functions, *National Bureau of Standards: Applied Mathematics Series,* Vol. 55, 1964.

[37]. M. E. Peskin, D. V. Schroeder, An Introduction to Quantum Field Theory, *Westview Press*, 1995.

[38]. Z. S. Sacks, D. Rozas, G. A. Swartzlander, Holographic formation of optical-vortex filaments, *J. Opt. Soc. Am. B*, Vol. 15, Issue 8, 1998, pp. 2226–2234.

[39]. J. Leach, M. R. Dennis, J. Courtial, M. J. Padgett, Vortex knots in light, *New J. Phys.*, Vol. 7, 2005, 55.

[40]. A. Ya. Bekshaev, M. S. Soskin, M. V. Vasnetsov, Optical vortex symmetry breakdown and decomposition of the orbital angular momentum of light beams, *J. Opt. Soc. Amer. A*, Vol. 20, Issue 8, 2003, pp. 1635–1643.

[41]. A. Mourka, J. Baumgartl, C. Shanor, K. Dholakia, E. M. Wright, Visualization of the birth of an optical vortex using diffraction from a triangular aperture, *Opt. Express*, Vol. 19, Issue 7, 2011, pp. 5760-5771.

[42]. V. Denisenko, V. Shvedov, A. Desyatnikov, D. Neshev, W. Krolikowski, A. Volyar, M. Soskin, Y. S. Kivshar, Determination of topological charges of polychromatic optical vortices, *Opt. Express*, Vol. 17, Issue 26, 2009, pp. 23374-23379.

[43]. A. Ya. Bekshaev, M. S. Soskin, M. V. Vasnetsov, Transformation of higher-order optical vortices upon focusing by an astigmatic lens, *Opt. Commun.*, Vol. 241, Issues 4–6, 2004, pp. 237–247.

[44]. A. Ya. Bekshaev, A. I. Karamoch, Astigmatic telescopic transformation of a high-order optical vortex, *Opt. Commun.*, Vol. 281, Issue 23, 2008, pp. 5687–5696.

[45]. F. W. J. Olver, Introduction to Asymptotics and Special Functions, *Academic Press*, 1975.

[46]. A. Ya. Bekshaev, O. V. Orlinska, Transformation of optical vortex beams by holograms with embedded phase singularity, *Opt. Commun.*, Vol. 283, Issue 7, 2010, pp. 1244–1250.

Appendix

Under the WDP conditions, it is suitable to represent Eq. (13.4) in the form

$$u(x,y,z) = u^I(x,y,z)$$

$$-\frac{k}{2\pi i z}\int_{-\infty}^{\infty} dy_a \int_{a}^{\infty} dx_a\, u_a(x_a,y_a)\exp\left\{\frac{ik}{2z}\left[(x-x_a)^2 + (y-y_a)^2\right]\right\}, \qquad (13.A1)$$

where $u^I(x,y,z)$ describes the complex amplitude distribution of an unperturbed beam (what had occurred in the observation plane if the screen were absent), and for $a \gg b$, $a \gg b_c$ the integral can be evaluated by means of the asymptotic analysis [45].

Let us start with considering the LG beam diffraction, then $u^I(x,y,z)$ $= u^{LG}(x,y,z_c + z)$ (cf. Eq. (13.9)) while, in the integral in the right-hand side of Eq. (13.A1), the expression (13.9) enters immediately. Then, omitting the coordinate-independent multipliers of Eq. (13.9), the integral in Eq. (13.A1) acquires the form

$$\exp\left[\frac{ik}{2z}(x^2+y^2)\right]\int_{-\infty}^{\infty} dy_a\, P(y_a,y,z_c - iz_{Rc})$$

$$\times \int_{a}^{\infty} dx_a\,(x_a + i\sigma y_a)^{|m|}\, P(x_a,x,z_c - iz_{Rc}), \qquad (13.A2)$$

where

$$P(x_a,x,d) = \exp\left[\frac{ikx_a^2}{2}\left(\frac{1}{d}+\frac{1}{z}\right) - \frac{ik}{z}xx_a\right]. \qquad (13.A3)$$

Under conditions of WDP, the sought OV cores' positions are close to the beam axis, so one can assume

$$x \simeq y \simeq 0, \tag{13.A4}$$

and neglect the summands proportional to x^2 and y^2 when compared to the coordinate-independent terms but retain the terms in the first degree in x. Further, for large a, the internal integral in Eq. (13.A2) can be estimated with the help of an asymptotic formula valid for arbitrary function $f(x)$:

$$\int_a^\infty f(x) \exp(iKx^2) dx \simeq \frac{i}{2K} \frac{f(a)}{a} \exp(iKa^2) + O\left(\frac{1}{a^2}\right). \tag{13.A5}$$

Consequently,

$$\int_a^\infty dx_a \left(x_a + i\sigma y_a\right)^{|m|} P\left(x_a, x, z_c - iz_{Rc}\right) \simeq \frac{iP\left(a, x, z_c - iz_{Rc}\right)}{ak\left(\dfrac{1}{z_c - iz_{Rc}} + \dfrac{1}{z}\right)} \left(a + i\sigma y_a\right)^{|m|}, \tag{13.A6}$$

and the external integral of Eq. (13.A2) is estimated by the method of stationary phase [45] which in connection with condition (13.A4) gives

$$\int_{-\infty}^\infty dy_a \left(a + i\sigma y_a\right)^{|m|} P\left(y_a, y, z_c - iz_{Rc}\right) \simeq \sqrt{\frac{2\pi i}{k\left(\dfrac{1}{z_c - iz_{Rc}} + \dfrac{1}{z}\right)}} \, a^{|m|}. \tag{13.A7}$$

Hence, we obtain the final representation for the integral term in the right-hand side of Eq. (13.A1):

$$-\frac{(-i)^{|m|+1}}{\sqrt{|m|!}} \sqrt{\frac{i}{2\pi}} \frac{k}{z} \left(\frac{z_{Rc}}{z_c - iz_{Rc}}\right)^{|m|+1} \left[k\left(\frac{1}{z} + \frac{1}{z_c - iz_{Rc}}\right)\right]^{-3/2} \frac{a^{|m|-1}}{b_0^{|m|}} P\left(a, x, z_c - iz_{Rc}\right) \; . \tag{13.A8}$$

The first term of Eq. (13.A1), with allowance for the near-axis condition (13.A4), reads

$$u^I(x,y,z) = u^{LG}(x,y,z_c + z) \simeq \frac{(-i)^{|m|+1}}{\sqrt{|m|!}} \left(\frac{z_{Rc}}{z_c + z - iz_{Rc}}\right)^{|m|+1} \left(\frac{x + i\sigma y}{b_0}\right)^{|m|}. \tag{13.A9}$$

Now, gathering all terms of Eq. (13.A1) and omitting the common coordinate independent multiplier $\dfrac{b_0}{\sqrt{|m|!}} \left(-\dfrac{iz_{Rc}}{b_0}\right)^{|m|+1}$, we find the asymptotic representation of the diffracted beam's complex amplitude distribution (13.26), (13.27).

In case of the Kummer beam diffraction, in Eq. (13.A1) $u^I(x,y,z)=u^K(x,y,z_h+z)$, and due to Eq. (13.6) and equations of Ref. [34] and the near-axis condition (13.A4),

$$u^K(x,y,z_h+z) \simeq \frac{z_e}{z+z_h}\sqrt{\frac{\pi}{2^{3|m|}}}(-i)^{|m|+1}\frac{z_R^{|m|+1}}{z_e^{|m|/2}(z_e-iz_R)^{|m|/2+1}}\left(\frac{x_e+i\sigma y_e}{b}\right)^{|m|}, \quad (13.A10)$$

where

$$z_e=\frac{z+z_h}{1+(z+z_h)/R}, \quad x_e=x\frac{z_e}{z+z_h}, \quad y_e=y\frac{z_e}{z+z_h}.$$

In the integrand of Eq. (13.A1), we use the asymptotic expression for the Kummer beam amplitude (13.6) valid for $(x_a^2+y_a^2)/b^2 \gg 1$,

$$u_a(x_a,y_a)=\frac{z_{he}}{z_h}\left(\frac{x_a+i\sigma y_a}{\sqrt{x_a^2+y_a^2}}\right)^{|m|}\left\{|m|(-i)^{|m|+1}\frac{z_{he}}{k(x_{ae}^2+y_{ae}^2)}\exp\left[\frac{ik}{2z_h}(x_a^2+y_a^2)\right]\right.$$

$$\left.+\frac{i}{2^{2|m|}}\frac{z_R^{2|m|+1}}{z_{he}^{|m|}(z_{he}-iz_R)^{|m|+1}}\exp\left[\frac{i}{2}\frac{k}{z_{he}-iz_R}(x_{ae}^2+y_{ae}^2)+\frac{ik}{2(z_h+R)}(x_a^2+y_a^2)\right]\right\}. \quad (13.A11)$$

This expression is similar to the formal asymptotic of the Kummer function [46] modified with account for the non-zero wavefront curvature of the incident Gaussian beam [14]; however, in the considered range of $(x_a^2+y_a^2)/b^2 \simeq 10$, the formal asymptotic expansion is not sufficiently accurate. To improve the approximation, the numerical coefficient in the second line of the asymptotic (13.A11) is modified, from $-2^{-|m|}i$ in [45], to $2^{-2|m|}i$ in Eq. (13.A11); validity of this correction was checked numerically.

Now both summands of (13.A11) should be substituted into the integral term of Eq. (13.A1). The first summand yields the corresponding summand of the integral term, which with omitted coordinate-independent coefficients obtains the representation (cf. the expression (13.A2))

$$\exp\left[\frac{ik}{2z}(x^2+y^2)\right]\int_{-\infty}^{\infty}dy_aP(y_a,y,z_h)\int_a^{\infty}dx_a\frac{(x_a+i\sigma y_a)^{|m|}}{(x_a^2+y_a^2)^{|m|/2+1}}P(x_a,x,z_h), \quad (13.A12)$$

where function $P(x_a,x,z_h)$ is defined in Eq. (13.A3). Then, via the corresponding analogs of Eqs. (13.A6) and (13.A7), we obtain

$$\int_a^\infty dx_a \frac{(x_a + i\sigma y_a)^{|m|}}{(x_a^2 + y_a^2)^{|m|/2+1}} P(x_a, x, z_h) \simeq \frac{iP(a,0,z_h)}{ak\left(\frac{1}{z_h} + \frac{1}{z}\right)} \frac{(a + i\sigma y_a)^{|m|}}{(a^2 + y_a^2)^{|m|/2+1}}, \quad (13.A13)$$

$$\int_{-\infty}^\infty dy_a \frac{(a + i\sigma y_a)^{|m|}}{(a^2 + y_a^2)^{|m|/2+1}} P(y_a, y, z_h) \simeq \sqrt{\frac{2\pi i}{k\left(\frac{1}{z_h} + \frac{1}{z}\right)}} \frac{1}{a^2}, \quad (13.A14)$$

and, after restoring the coordinate-independent coefficients, arrive at the total contribution of the first summand of (13.A11) to the integral term of Eq. (13.A1)

$$|m|(-i)^{|m|+1} \sqrt{\frac{i}{2\pi}} \frac{z_h}{z} \left[k\left(\frac{1}{z_h} + \frac{1}{z}\right) \right]^{-3/2} \frac{1}{a^3} P(a, x, z_h). \quad (13.A15)$$

Similar operations with the second summand of Eq. (13.A11) lead to the expression (cf. Eqs. (13.A2) and (13.A12))

$$\exp\left[\frac{ik}{2z}(x^2 + y^2)\right] \int_{-\infty}^\infty dy_a P(y_a, y, z_d) \int_a^\infty dx_a \frac{(x_a + i\sigma y_a)^{|m|}}{(x_a^2 + y_a^2)^{|m|/2}} P(x_a, x, z_d), \quad (13.A16)$$

where

$$\frac{1}{z_d} = \frac{1}{z_{he} - iz_R} \left(\frac{z_{he}}{z_h}\right)^2 + \frac{1}{z_h + R}, \quad (13.A17)$$

which, finally, results in the following contribution to the integral term of Eq. (13.A1):

$$-\frac{ik}{2^{2|m|}} \sqrt{\frac{i}{2\pi}} \frac{z_{he}}{zz_h} \frac{z_R^{2|m|+1}}{z_{he}^{|m|}(z_{he} - iz_R)^{|m|+1}} \left[k\left(\frac{1}{z_d} + \frac{1}{z}\right) \right]^{-3/2} \frac{1}{a} P(a, x, z_d). \quad (13.A18)$$

Then, combining Eqs. (13.A1), (13.A10), (13.A15) and (13.A18), we find the complex amplitude representation (13.18)–(13.21). Note that due to relation

$$\frac{1}{z_{he} - iz_R} \left(\frac{z_{he}}{z_h}\right)^2 + \frac{1}{z_h + R} = \frac{i}{kb^2(z_h)} + \frac{1}{R(z_h)},$$

expressions (13.A17) and (13.A18) contain the radius $b(z_h)$ and the wavefront curvature radius $R(z_h)$ that the initial Gaussian beam, incident onto the VG, would have possessed in the screen plane if it had propagated 'freely', without the VG-induced transformation.